Influence of Al-doping on the Structural and Electronic Properties of $NdNiO_3$ Thin Films

M.Sc. Thesis

By

Diptanshu Basak

DISCIPLINE OF PHYSICS

INDIAN INSTITUTE OF TECHNOLOGY INDORE

JUNE 2022

Influence of Al-doping on the Structure and Electronic Properties of $NdNiO_3$ Thin Films

A THESIS

Submitted in partial fulfilment of the
requirements for the award of the degree
of
Master of Science

by
Diptanshu Basak

DISCIPLINE OF PHYSICS
INDIAN INSTITUTE OF TECHNOLOGY INDORE
JUNE 2022

INDIAN INSTITUTE OF TECHNOLOGY INDORE

CANDIDATE'S DECLARATION

I hereby certify that the work which is being presented in the thesis entitled **Influence of Al-doping on the structural and electronic properties of $NdNiO_3$ thin films** in the partial fulfilment of the requirements for the award of the degree of **MASTER OF SCIENCE** and submitted in the **DISCIPLINE OF PHYSICS, Indian Institute of Technology Indore**, is an authentic record of my own work carried out during the time period from August 2020 to June 2022 under the supervision of Prof. Krushna R. Mavani, Discipline of Physics, Indian Institute of Technology Indore.

The matter presented in this thesis has not been submitted by me for the award of any other degree of this or any other institute.

Diptanshu Basak

Signature of the student
DIPTANSHU BASAK

This is to certify that the above statement made by the candidate is correct to the best of my/our knowledge.

Signature of the Supervisor of M.Sc. thesis
PROF. KRUSHNA R. MAVANI

Diptanshu Basak has successfully given his M.Sc. Oral Examination held on 3rd June, 2022.

Signature of Supervisor of MSc thesis
Date: 31.05.2022

Convener, DPGC
Date: 08/06/2022

Signature of PSPC Member 1
Prof. Preeti A. Bhobe
Date: 06.06.2022

Signature of PSPC Member 2
Dr. Somaditya Sen
Date: 6/6/2022

Dedicated to my Guardians and Teachers

ACKNOWLEDGEMENTS

I sincerely confess that my thesis work cannot be fulfilled without the effort of individuals. This project is the collective effort of many people to whom I will always be thankful for guiding me in a productive direction. I want to contribute my utmost effort to recall all the people and acknowledge them.

First and foremost, I am deeply indebted to Prof. Krushna R. Mavani, Department of Physics, Indian Institute of Technology, Indore, for making me a member of her "Thin film Laboratory," IIT Indore. Her invaluable suggestions and constant support kept me motivated throughout my project journey. I am incredibly mesmerized after seeing her foresight in research work. Her prodigious knowledge and logical approach always encouraged me to dig out any research problem and kept me on the right track to complete my current MSc. project thesis. I also want to express my sincere gratitude to my PSPC members, Prof. Preeti A. Bhobe and Dr. Somaditya Sen, for their valuable suggestions and motivations.

I am greatly obliged to my lab partners for supporting me throughout the project. Their hard work has inspired me to get fresh enthusiasm for my progress in project work. I would like to dedicate my special thanks to Ms. Ekta Yadav for helping me in sample preparation, sample characterization, data plotting, and data analysis. I would also like to express my respect to Ms. Ekta Yadav and Mr. Ketan Navale for helping me to understand the basic concepts of my project work. I want to thank Ms. Ekta Yadav, Ms. Komal Pathy, Mr. Ketan Navale, Mr. Manish Kumar, and Mr. Udit Kumar for their love and moral support during my work. I would also like to thank all the faculty members and staff members of Discipline of Physics, IIT Indore, for their help and support.

As expected in everyone's life, friends played an essential role in every phase of my first hostel life. In the end, my life is indebted to my

parents for nurturing me from my childhood, and I would like to thank them for playing the role of **“Friend, Philosopher, and Guide.”**

Diptanshu Basak

Abstract

$NdNiO_3$ is well-known in the scientific world for its metal to insulator transition (MIT), which can be used in ultrafast switches, photovoltaics, temperature sensors, and other applications. We have synthesized Al-doped $NdNiO_3$ thin films on LAO (001) single crystal substrate using pulsed laser deposition (PLD) technique with varying doping percentages. To check the phase purity, X-ray diffraction (XRD) has been performed. Both room-temperature, and temperature-dependent Raman data have been recorded to explore phonon modes and a temperature study of resistivity has been performed to investigate the MIT of the sample. $NdNiO_3$ exhibits a metal-to-insulator phase at ~ 75K, and the transition temperature increases with Al doping. 20% Al-doped $NdNiO_3$ thin film shows complete insulating behavior below room temperature. Raman data suggests the octahedral distortion and charge ordering in NiO_6 octahedra which assist to explain the insulating behavior of the sample.

TABLE OF CONTENTS

Chapter 3: Results and Discussions

LIST OF FIGURES

LIST OF TABLES

ABBREVIATION

Transition metal oxides	TMOs
Physical Vapour Deposition	PVD
Chemical Vapour Deposition	CVD
Molecular Beam Epitaxy	MBE
Pulsed Laser Deposition	PLD
$NdNiO_3$	NNO
$LaAlO_3$	LAO
Upper Hubbard Band	UHB
Lower Hubbard Band	LHB
Metal Insulator Transition	MIT
X-ray diffraction	XRD

Chapter 1
Introduction

Nowadays, thin films, nanomaterials, fabrication techniques, and their applications provide the domain of active research [1]. Scientists have been trying to modify the gadgets by reducing their size and enhancing their functionality in recent times, and its successful implementation is thin films. Thin films are multilayered films with a thickness of several nanometres deposited on the substrate. Thin films have various optical, electrical, magnetic, chemical, and mechanical applications, such as reflective/antireflective coatings, interference filters, compact discs (CD) semiconductor devices, memory discs, gas/liquid sensors, tribological coatings, ultrafast switches *etc* [1]. Here, transition metal oxides (also known as complex oxides), which are one of the categories of Perovskites, serve as a promising material for the new generation of technology for enhanced functions compared to Si-based technology and empower our technology with Mott Electronics [2].

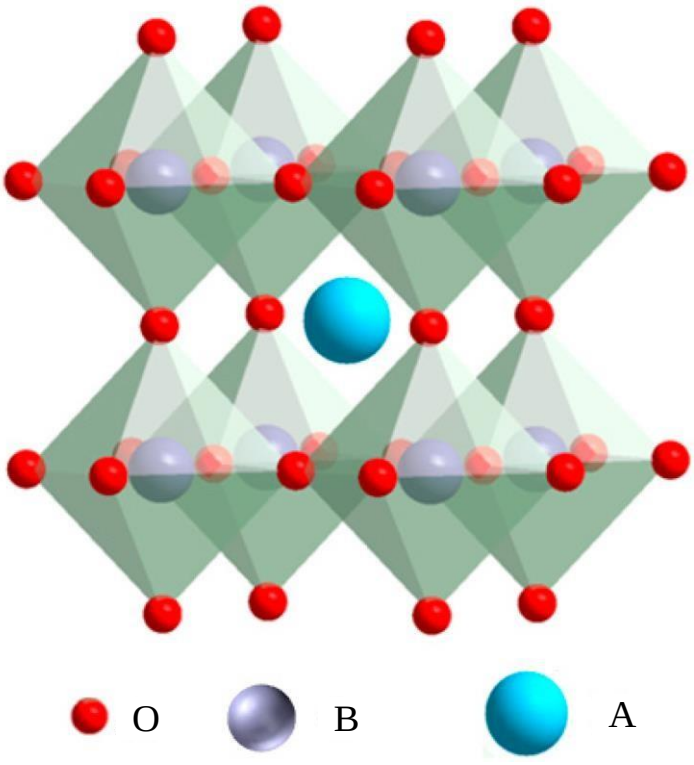

Figure 1.1: Ideal ABO_3 cubic perovskite [3]

The first Perovskite $CaTiO_3$ was discovered by Gustov Rose in the Ural Mountains of Russia in 1839 [4]. Perovskite oxides exhibit

intriguing properties due to the mutual interplay of lattice, charge, orbital, spin degrees of freedom. The most investigated perovskite oxides are Rare Earth Cuprates ($RCuO_3$) for high-temperature superconductivity, Rare Earth Nickelates ($RNiO_3$) for Colossal Magnetoresistance (CM), and layered Rare Earth Manganates ($RMnO_3$) for Giant Magnetoresistance (GM).

Generally, transition metal oxides possess the structural formula ABO_3, where A represents the larger cation belonging mostly to rare-earth ions, B represents a comparatively smaller transition metal ions, and O stands for oxygen as the anion. In the ideal crystal structure, A ion is surrounded by 8 BO_6 octahedra at the corners of a cubic cell, shown in figure 1.1. Due to the larger size of the A ion, the Goldschmidt tolerance factor is significant in these transition metal oxides. This tolerance factor can be represented by the following formula:

$$t = \frac{R_A + R_O}{\sqrt{2}(R_B + R_O)}$$

Here, R_A, R_B, and R_O represent the radius of A, B, and O ions, respectively.

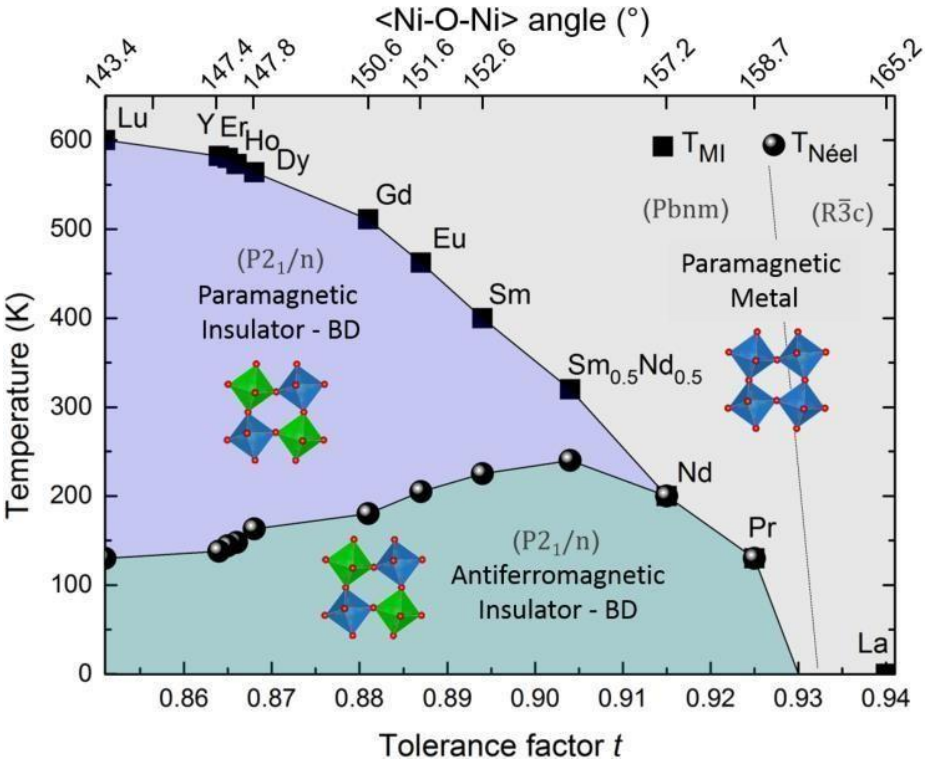

Figure 1.2: Phase diagram of $RNiO_3$ compounds [5]

In the ideal perovskite structure, the value of the tolerance factor is one [6]. There will be a marginal reduction of tolerance factors with reducing A-ion size, which causes diminished structural stability. This decrement in size creates a vacancy in the crystal structure which can be filled up by distorting BO_6 octahedra. Greater distortion results in the reduction of the B-O-B bond angle, consequently the increment in tilt angle. This reduces the overlap between d- and p- orbitals in the octahedra and increases the band gap between them. This distortion is called octahedral distortion. Thus for the high value of the tolerance factor (which lies between 0.75 and 1) [7], these oxides are primarily stable and can be used for further exploration, such as structural modification, and chemical substitution [8]. The phase diagram of $RNiO_3$ materials (Figure 1.2) clearly shows that $LaNiO_3$ is a paramagnetic metal with a rhombohedral structure at all temperatures. Electronic (from metal to insulator), magnetic (paramagnetic to antiferromagnetic), and structural (orthorhombic to monoclinic) phase transitions all occur at the same temperature for $PrNiO_3$ and $NdNiO_3$ [9]. For the rest of the rare earth nickelates, electronic transitions occur at high temperatures, whereas magnetic changes occur at relatively low temperatures.

Besides octahedral distortion, another geometrical distortion occurs in BO_6 octahedra to stabilize the structure with low energy. Suppose an electron has more than one option of choosing a state with the same energy, the energy of the system costs higher. In order to reduce the overall energy expenses of that system, the structure undergoes distortion to allocate the electron to a particular energy state lowering the symmetry of the system. In particular, five degenerate energy states are available for d-orbital electrons in octahedra, and due to crystal field splitting, the states split into three t_{2g} (lower energy) and two e_g (higher energy) orbitals. In the case of transition metal ions with d^1, d^2, d^4, d^6, d^7 (high spin), and d^9 configurations, more than one energy states are attainable for the last electron. In order to avoid further the state of confusion, the states rearrange themselves (Figure 1.3) by out-

of-plane octahedral compression or elongation so that the energy of the whole system minimizes. The octahedra extension and contraction along the Z-axis are referred to as z-out distortion and z-in distortion, respectively, as shown in figure 1.4 and this phenomenon is called **Jahn-Teller distortion** [10]. This distortion is robust in the case of unevenly occupying e_g orbital than t_{2g} orbital. For example, Jahn-Teller distortion was strongly observed in $RMnO_3$ with Mn^{3+} ($t_{2g}^{3}\ e_{g}^{1}$) and La_2CuO_4 with Cu^{2+} oxidation state ($t_{2g}^{6}\ e_{g}^{3}$) [11].

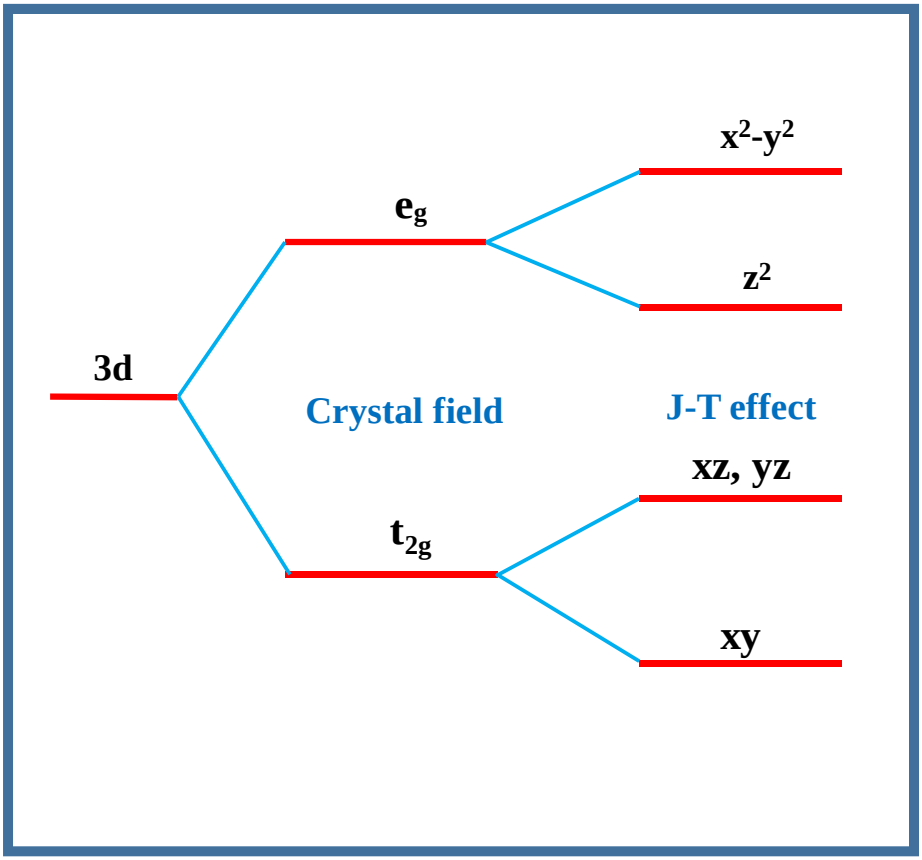

Figure 1.3: Effect of Crystal field splitting and Jahn-Teller distortion in 3d-orbital

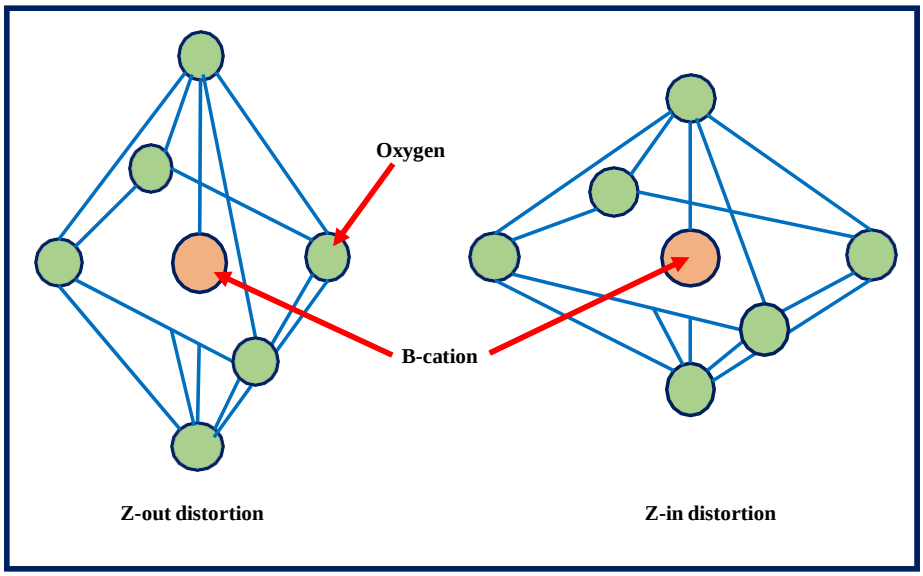

Figure 1.4: z-out and z-in distortion of BO_6 octahedral due to Jahn-Teller distortion

1.1 $RNiO_3$ bulk and thin films:

Among various transition metal oxides, $RNiO_3$ perovskites are renowned for their sharp metal to insulator transition. Here R represents rare-earth ions such as La^{3+}, Pr^{3+}, Nd^{3+}, Sm^{3+}, *etc.* Conduction in the metallic state supports the hybridization between Ni 3d and O 2p orbitals. Nickelates are very difficult to synthesize, especially when the R ion is too small, as it needs high temperature and high pressure to stabilize the Ni^{3+} ionic state. In the beginning, most of the research was performed with bulk polycrystalline nickelates. But the bulk form of the sample does not exhibit single-phase nature. Presently, we can efficiently synthesize the single phase form of nickelates through thin film synthesis. We can easily deposit thin films of several nanometers on a single crystal substrate through the processes such as thermal evaporation, chemical deposition, evaporation by irradiation of the source [12]. This growth process depends mainly on the nucleation process followed by different development stages. Nucleation is the bombardment of electrons and ions on the surface of substrates. The development stages can be classified into the following points:

1. Island growth (Volmer-Weber)

2. Layer by layer growth (Frank-van der Merwe)
3. Mixed growth (Stranski-Krastanov)

Mixed growth can be formed by layer by layer growth followed by 2D island formation. These growth processes show lots of valuable features:

A. Various deposition conditions such as growth temperature and growth rate modulate thin films' nucleation and growth stages.
B. Phase and orientation of the films can be controlled by the deposition conditions as well as the crystal structure of the substrate.

Various deposition techniques are available for thin-film synthesis:

1) DC sputtering.
2) Magnetron sputtering.
3) Pulsed laser deposition.
4) Sol-gel method.
5) Molecular beam epitaxy.

Among these techniques, we have preferred the pulsed laser deposition (PLD) technique to synthesize our thin films, as elaborated in chapter 2.

1.2 Electrical Transport:

Electrical transport of a particular material is defined as how much current passes through the material after applying a specific voltage. In a broad sense, two types of materials named metals and insulators represent the contrast in the conductivity range. The conductivity of metals is in the order of $10^{9}\ \Omega^{-1}\ cm^{-1}$, whereas for typical non-metals, it is in the order of $10^{-18}\ \Omega^{-1}\ cm^{-1}$. If we speak about the standard definition of metal and insulator, then at absolute 0K temperature, metals exhibit finite conductivity, and at the same place, insulators show zero conductivity. $RNiO_3$ exhibits both metallic and insulating behavior in a particular temperature range. To find the transition from metal to insulator, we can easily focus on the ($d\rho/dT$)

value. In the insulating state, this value is less than zero, *i.e.*, with decreasing temperature, the value of resistivity increases, and contrarily, the metallic state exhibits $(d\rho/dT) > 0$. The evolution of various models to find the exact explanation of the conductivity of $RNiO_3$ is given below [13]:

a) Free electron model:

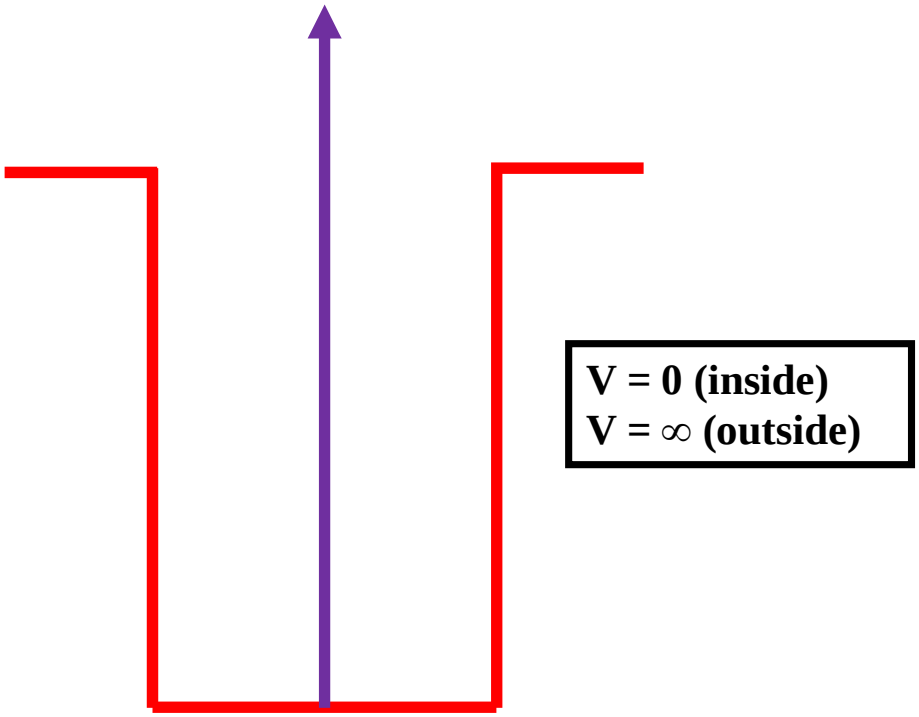

Figure 1.5: Schematic of infinite potential well for free electrons considering infinite potential at the surface and zero otherwise

In 1927, Paul Drude proposed the "Free electron model," [14] which successfully explained the behavior of electrons in the materials. In this model, electrons are considered as non-interacting free gas particles experiencing the potential (Figure 1.5) on the surface of the metal. Paul Drude considered some assumptions to complete this model:

1. Electrons, according to this model, are non-interacting.
2. Inside metals, electrons are entirely free to move.
3. Positive ions are immobile inside the metals.
4. There is no positive potential for the ions in the lattices.

5. Electrons undergo instantaneous, continuous collision among themselves.

The electric conductivity of metal in the presence of an external electric field is given as:

$$\sigma = \frac{ne^2\tau}{m} \qquad \text{----- (1.1)}$$

where, n is the free electron density, r is known as relaxation time, the average time between two consecutive collisions, e is the charge of an electron, and m is the electron mass.

The Drude model successfully explained ohm's law, DC, AC, and thermal conductivities, the Hall effect, and magnetoresistance in metals near room temperature. Additionally, this model partly explains the Weidemann-Franz law of 1853. However, this model overestimates the electronic heat capacity of metals and cannot explain heat capacity, temperature-dependent resistivity, and the sign of Hall coefficient for certain metals. Also, this model can not distinguish between metals and insulators. This model was partially improved in 1927 by Arnold Sommerfeld, who combined the classical Drude model with quantum mechanical Fermi–Dirac statistics, and hence it is also known as the Drude–Sommerfeld model. Here electrons are considered as quantum particles, and we can easily apply Schrödinger's equation in this model. This model effectively describes the Wiedemann-Franz law related to electrical and thermal conductivity, temperature-dependent resistivity, electron heat capacity, the shape of the electronic density of states, and paramagnetic susceptibility, but still, it fails to distinguish between metal, semiconductor, and insulator.

b) Band Theory for Solids:

This theory is also called the nearly free electron theory. The free electron model was stuck due to the ignorance of electrons and ions interactions, but in actuality, the electron motion is complicated in the lattice, and we can not ignore the potential due to the lattice field. In band theory, we consider the average periodic potential with a period of

lattice constant "a" in the solid. The potential can be represented as V(x+a) = V(x). Though the actual potential is parabolic, according to the Kroning-Penny model (KP model), we can consider the potential as a rectangular pulse. From the Bloch theorem, we can consider the possible solution as:

$$\psi(x) = e^{-ik.x} u_k(x) \text{----------(1.2)}$$

where, $u_k(x)$ is a periodic function, k is the wave vector of the electron. Incorporating this potential and wave function into the one dimensional Schrödinger equation, which is given by:

$$[-\frac{\hbar^2}{2m}\frac{d^2}{dx^2} + V(x)]\,\psi(x) = E\,\psi(x), \text{---------} (1.3)$$

we can easily get the relation between wave vector k and energy E. It comes out as:

$$\cos(ka) = \cos(\alpha a) + P\frac{\sin(\alpha a)}{\alpha a} \qquad \text{----- (1.4)}$$

where, $\alpha^2 = \frac{8\pi^2 mE}{h^2}$ and $P = \frac{4\pi^2 mVba}{h^2}$ is constant with 'b' as barrier width and 'a' as the period of the lattice. As the value of $\cos(ka)$ lies between -1 to +1, this relation imposes a constraint in energy states, i.e., we can find energy regions where wave functions do not satisfy the conditions. These forbidden energy regions are called band gaps of solid. We can classify the materials into metals, semiconductors, and insulators depending on the band gaps. Metals do not exhibit any bandgap; however, insulators possess a wide bandgap in the range of several eV. The bandgap remains less at low temperatures in the semiconductors, and these semiconductors behave metallically at higher temperatures (Figure 1.6).

Although the band theory got the victory after classifying metal, insulator, and semiconductor from their conduction mechanism, this model is unable to clarify the conduction mechanism of some oxides due to their insulating behaviour. Despite the band theory predicts the metallic nature of a partially filled conduction band, some TMOs such as V_2O_3, Fe_3O_4, NiO, *etc.* exhibit an insulating state unexpectedly [15].

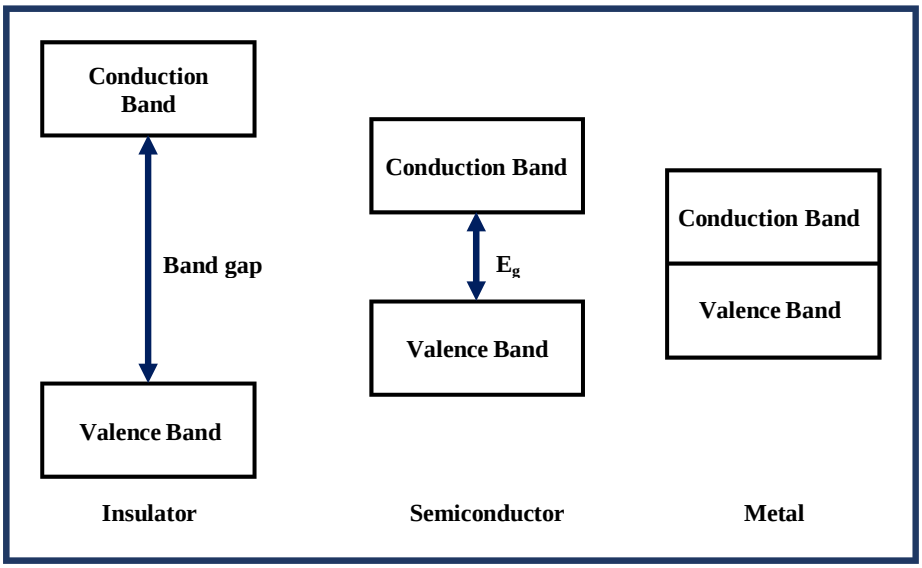

Figure 1.6: Schematic of bands in metal, semiconductor and insulator and variation in their band gaps

c) Mott-Hubbard model:

As band theory did not consider the electron-electron repulsion, it failed to explain the insulating behavior of some oxides such as NiO, V_2O_3, Fe_3O_4, *etc.* N. F. Mott was the man who first evoked the possibility of electron localization due to Coulomb interaction between them. Later the theoretical interpretation of this possibility was successfully given by Hubbard, and according to this model, the Hubbard Hamiltonian can be written as:

$$H = -t\sum_{\langle i,j\rangle,\sigma}(c^{\dagger}_{i,\sigma} c_{j,\sigma} + hc) + U\sum_{i=1}^{N} n_{i\uparrow}n_{j\downarrow} \quad \text{----- (1.5)}$$

where, U is the on-site Coulomb interaction energy, t is the hopping integral, $c^{\dagger}_{i,\sigma}$ and $c_{j,\sigma}$ are creation and annihilation operators [16]. This Hamiltonian is the convergence of two contrasting terms:

a. the first term corresponds to kinetic energy to explain the metallic behavior, and
b. last is the Coulomb repulsion term where U is the potential energy experienced by keeping two electrons at one site, maintaining Pauli Exclusion Principle, and can be termed as:

$$U = E(d^{n+1}) + E(d^{n-1}) - E(d^{2n}) \text{---------(1.6)}$$

Due to the enormous energy cost in the strongly correlated oxides, the d-orbital splits into Upper Hubbard Band (UHB) and Lower Hubbard Band (LHB) (Figure 1.7). Depending on the spacing in these two bands, we can explain metallic and insulating behavior more precisely. We can also determine the conductivity by the strength of electron correlation U/t [17]. In the case of metals, U/t << 1, i.e., the on-site Coulomb repulsion is negligible, and for insulators, it is U/t >> 1, i.e., Coulomb repulsion is strong enough. These insulators with large bandgaps are called Mott-Hubbard insulators.

Though this model successfully explains the insulating nature of many TMOs, it is again failed to provide the explanation of the insulating nature of some TMOs consisting of Co, Ni, *etc.* [16] as well as the metallic state of some sulphides [18].

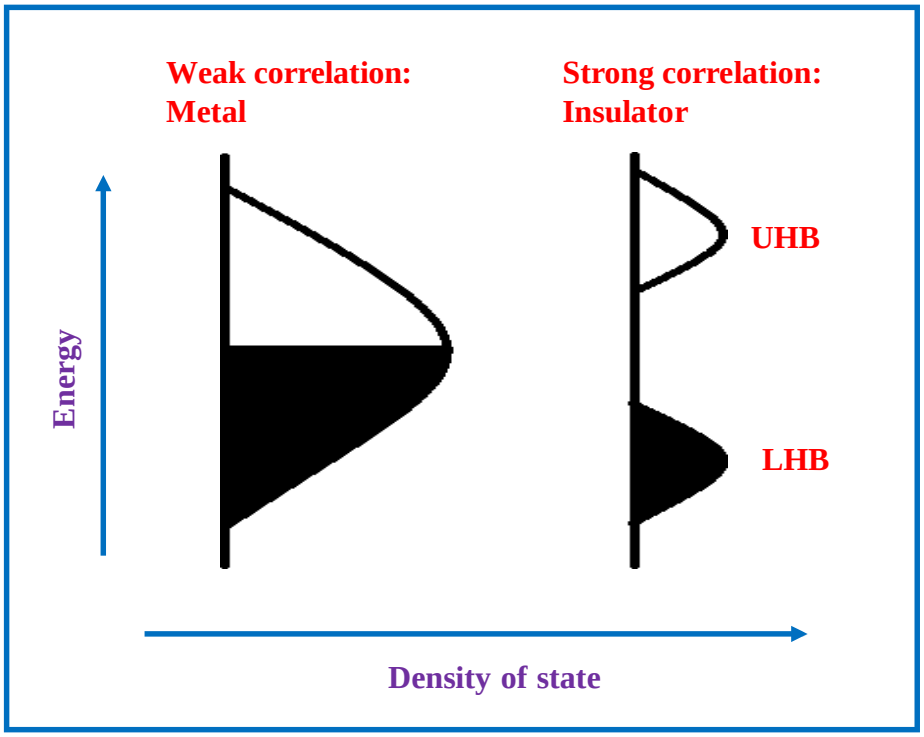

Figure 1.7: Schematic of energy vs density of states for a metal having half-filled d band caused by weak electron-electron correlation, and splitting of d band into LHB and UHB for an insulator due to strong correlation

d) Zaanen-Sawatzky-Allen model:

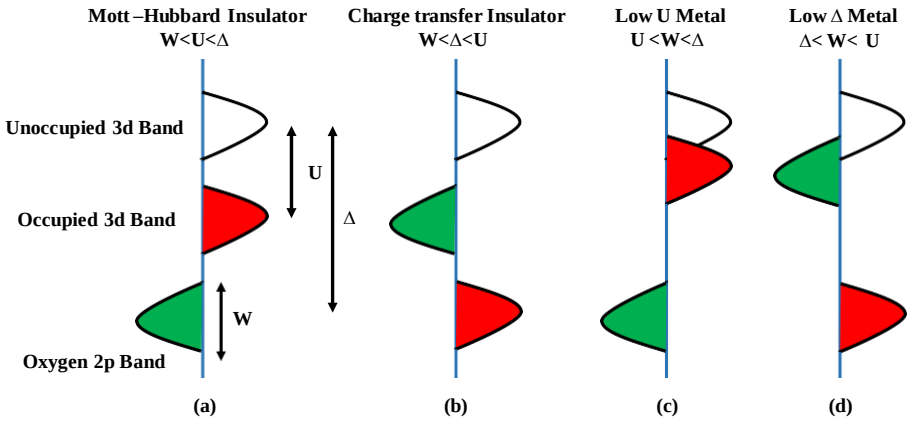

Figure 1.8: Schematic for ZSA framework showing two types of insulator: a) Mott –Hubbard Insulator, b) charge transfer insulator, and two types of metals: c) low U metal, d) low Δ metal

In the previous model, considering the bandgap between LHB and UHB, we can easily explain the charge fluctuation of the following type:

$$d_i^n d_j^n \rightarrow d_i^{n-1} d_j^{n+1};$$

however, it fails to explain the charge fluctuations such as $d_i^n \rightarrow d_i^{n+1}\underline{L}$ type, where $\underline{L}$ is a legend hole. Zaanen, Sawatzky, and Allen constructed a framework known as the ZSA framework (Figure 1.8) that consists of three parameters [19]:

a. Coulomb repulsion energy (U), the energy difference between unoccupied UHB and occupied LHB,
b. Bandwidth (W), and
c. charge-transfer gap (Δ), the energy difference between the unoccupied d and p bands.

This framework explains the conductivity of transition metal oxides, halides, and sulfides. Depending on these parameters, we can classify the insulators and metals in the following four categories:

a. **Mott-Hubbard insulators (W < U < Δ):** In this category, the energy difference between unoccupied and occupied d bands (U) is lower than that between unoccupied d band and filled p band, e.g., V_2O_3, Ti_2O_3.
b. **Charge transfer insulators (W < Δ < U):** The energy difference Δ is lower than U in this case. CuO, $RNiO_3$ compounds such as $PrNiO_3$ and $NdNiO_3$ fall into this category [13].
c. **Low Δ metals:** Here, Δ < W and the unoccupied d band and p band overlap in this case.
d. **Low U metals:** Here, U < W and the unoccupied and occupied d bands overlap in this case.

1.2.1 Possible Reason of Metal to Insulator Transition:

Metal to Insulator transition is one of the fascinating phenomena in transition metal oxides (TMOs), especially in rare earth nickelates ($RNiO_3$). This transition can be controlled by various external parameters such as doping, pressure, temperature, external field, and dimensionality change. Many assumptions can be estimated to explain the reasons behind MIT that are also responsible for changing the states. These assumptions are also based on the previous conduction models.

(a) MIT due to band manipulation:

In insulators, localization of charge carriers occurs in the large energy gap between the valence and conduction bands. By manipulating the bands, we can achieve the transition from insulating to the metallic state in two different ways:

1. We can control the carrier concentration of bands, called band filling. Here, the valence and conduction bands can be filled partially by supplying extra electrons and holes into the system. We can also control this by varying oxygen stoichiometry. In the case of rare earth nickelates, CMR manganites, high T_c cuprates, carrier concentration variation is more effective in controlling MIT that can be achieved by varying doping concentration.

2. Besides controlling carrier concentration, we can manipulate the relative positions of valence and conduction bands, and the metallic state can be achieved by closing this energy gap.

(b) MIT due to Charge ordering:

One of the most exciting reasons behind MIT of $RNiO_3$ is charge ordering. In this phenomenon, the charge of nickel ions at different lattice sites differs in a particular manner due to the tendency of possessing multiple valence states. Above metal to insulator transition temperature (T_{MI}), Ni-ions in every lattice site possess 3+ valance states, and below T_{MI}, the charges in Ni-ions order to 2+/4+ valence states. This charge ordering is accompanied by orbital or magnetic ordering and results in structural changes. In the case of structural change from orthorhombic to monoclinic structure, unit cell volume increases to 0.2%.

1.2.2 Conduction Mechanisms:

Electronic transport in solids such as metals and insulators strongly depends upon the temperature and the behavior of temperature dependency acts differently regarding to the types of solids.

Conduction mechanism in metals:

In the classical point of view, the resistivity of metal attributes due to the following parameters:

a) Phonon-electron interaction,
b) Impurity, imperfection, disorder-induced defect.

Keeping these parameters in our mind, we can formulate the resistivity in the following manner:

$$\rho_{total} = \rho_{phonon} + \rho_{defect}$$

Resistivity due to disorder does not depend upon temperature, but the resistivity contributed by electron-phonon interaction or phonon scattering linearly depends on temperature that provides the following mathematical expression:

$$\rho_{phonon} \propto \frac{\hbar^2 \pi}{kM} \frac{T}{\theta^2} \quad \text{----- (1.7)}$$

In the above expression, k corresponds to the Boltzmann constant, M represents the mass of the ion, and θ signifies Debye frequency. Accordingly, the phonon-electron interaction dominates at the higher temperature and the total resistivity overall depends upon temperature linearly. However, at the lower temperature, the value of ρ_{phonon} is infinitesimal and the dominating part of total resistivity is ρ_{defect} that varies constantly with temperature.

However, the above theory does not support the experimental results. The reason behind this disagreement is the ignorance of the mutual interaction of electrons. In 1956, Soviet physicist Lev Landau incorporated the concept of mutual interaction of fermions and showed the quadratic dependency of temperature with resistivity. This modified picture of conductivity is known as classical Landau picture or mostly pronounced as Fermi liquid behavior. The mathematical expression supporting this model can be represented by:

$$\rho_{total} = \rho_0 + AT^2 \text{ -------} (1.8)$$

where, ρ_0 is the residual resistivity which occurs due to the lattice - imperfections, grain boundary, dislocations, defects and the constant A signifies electron-electron interaction. This model is valid in the low-temperature metallic state.

Conduction mechanism in insulators:

There are various models that describe the conductivity of insulating states in terms of activation energy, hopping energy, *etc.* in transition metal oxides. Some of these models are described below.

Arrhenius Model:

Thermally activated band conduction is the most prevalent conduction process in semiconducting substances at sufficiently high temperatures. Thermal energy is sufficient to shift charge carriers from the valance band to the conduction band at high temperature, and the Arrhenius equation describes the temperature dependence of resistivity by the following equation:

$$\rho = \rho_0 \exp\left(\frac{\Delta}{k_B T}\right) \quad \text{----- (1.9)}$$

where, Δ represents the activation energy for conduction, and k_B corresponds to Boltzmann's constant. Following the above equation, if we plot the graph between ln ρ and 1/T, it is a straight line.

Conduction is aided by charge carrier hopping at lower temperatures, when thermal energy is less than the activation energy. This type of carrier hopping is known as nearest neighbour hopping since it is confined to the closest neighbours. Nearest neighbour hopping requires less activation energy than thermally induced band conduction. This type of conduction mechanism can be seen in materials that are disordered.

Variable range hopping:

Mott variable range hopping is another hopping method for conduction between the localized states (VRH). This Mott VRH conduction mechanism was first observed in amorphous semiconductors, but, interestingly, it was later discovered in various disordered insulators. When the thermal energy is insufficient to activate charge carriers across the gap between valence and conduction band at low temperatures, the VRH enables charge transfer. In this case, phonons in the lattice usually help in conduction via hopping. The hopping of charge carriers is more probable when the charge transfer states are closely spaced in the lattice and cost less energy to hop. Both prerequisites, however, are not always met. As the range of localized states and hopping energy are important in this conduction mechanism, the probability of hopping at low temperature can be represented as:

$$P \propto \exp(-\alpha R - \beta\Delta) \text{--------} (1.10)$$

where, the constant α can be related to localization length, R represents the spatial separation between two localized states and β is a constant which is inversely proportional to temperature and Δ exhibits hopping energy.

In comparison to states that are far apart, the energy difference between spatially closer states will be greater. As a result, electron hopping is preferable to the sites that are well separated in space as compared to the neighbouring sites. The hopping probability should be for the optimum value of R and Δ. The temperature dependent resistivity derived by Mott is as follows:

$$\rho = \rho_0 \, exp \left(\frac{T_0}{T}\right)^{\frac{1}{n+1}} \quad (1.11)$$

Here, n shows the dimension of the system, and T_0 is the characteristic temperature. The term T_0 depends on the density of states N (E) at the Fermi level maintaining the relation $k_B T_0 = \frac{18}{N(E)\alpha^3}$, where α is the localization length. In the three-dimensional case (n = 3), from the temperature dependent resistivity expression, we can easily see that ln ρ varies linearly with $T^{-1/4}$ according to this model.

1.3 Motivation:

To explore the structural change and transport characteristics of these thin films, the doping percentage, oxygen partial pressure, film thickness, and substrate type can all be varied. The electronic properties of $NdNiO_3$ via carrier injection due to aliovalent doping (both hole and electron doping) are well studied in the literature. However, there are no such reports available on the isovalent doping in nickelates. Therefore, we have studied Al-doping at the Ni-site in $RNiO_3$ thin films to investigate the effects of aliovalent dopant. Since the ionic radii of Nd^{3+} and Ni^{3+} ions are 1.27 Å and 0.6 Å, respectively, whereas the ionic radii of Al^{3+} ions are 0.535 Å, Al-ion can be easily doped at the Ni-site of $NdNiO_3$ thin films. We have studied the structural change and transport properties in our current investigation by varying the Al-ion doping percentage in $NdNiO_3$ thin films deposited on $LaAlO_3$ (LAO) single crystal substrates with (001) orientation.

References:

[1] Z. Yang, C. Ko, and S. Ramanathan, "Oxide electronics utilizing ultrafast metal-insulator transitions," *Annual Review of Materials Research*, vol. 41, pp. 337–367, Aug. 2011, doi: 10.1146/annurev-matsci-062910-100347.

[2] J. M. Rondinelli, S. J. May, and J. W. Freeland, "Control of octahedral connectivity in perovskite oxide heterostructures: An emerging route to multifunctional materials discovery," *MRS Bulletin*, vol. 37, no. 3, pp. 261–270, Mar. 2012, doi: 10.1557/mrs.2012.49.

[3] Q. Shen, S. Dong, S. Li, G. Yang, and X. Pan, "A review on the catalytic decomposition of no by perovskite-type oxides," *Catalysts*, vol. 11, no. 5. MDPI, May 01, 2021. doi: 10.3390/catal11050622.

[4] A. Navrotsky, "Energetics and Crystal Chemical Systematic among Ilmenite, Lithium Niobate, and Perovskite Structures," *Chemistry of Materials*, vol. 10, no. 10. American Chemical Society, pp. 2787–2793, 1998. doi: 10.1021/cm9801901.

[5] S. Catalano, M. Gibert, J. Fowlie, J. Iñiguez, J. M. Triscone, and J. Kreisel, "Rare-earth nickelates RNiO3: Thin films and heterostructures," *Reports on Progress in Physics*, vol. 81, no. 4. Institute of Physics Publishing, Feb. 14, 2018. doi: 10.1088/1361-6633/aaa37a.

[6] M. L. Medarde, "Structural, magnetic and electronic properties of perovskites (R = rare earth) Structural, magnetic and electronic properties of RNiO 3 perovskites (R = rare earth)," 1997. [Online]. Available: http://iopscience.iop.org/0953-8984/9/8/003

[7] M. A. Peña and J. L. G. Fierro, "Chemical structures and performance of perovskite oxides," *Chemical Reviews*, vol. 101, no. 7. pp. 1981–2017, Jul. 2001. doi: 10.1021/cr980129f.

[8] G. Catalan, "Progress in perovskite nickelate research," *Phase Transitions*, vol. 81, no. 7–8. pp. 729–749, Jul. 2008. doi: 10.1080/01411590801992463.

[9] A. Venimadhav, I. Chaitanya Lekshmi, and M. Hegde, "Strain-induced metallic behavior in PrNiO 3 epitaxial thin ®lms."

[10] D. Khomskii, *Transition metal compounds*.

[11] Y. E. Suyolcu *et al.*, "Octahedral Distortions at High-Temperature Superconducting La2CuO4 Interfaces: Visualizing Jahn–Teller Effects," *Advanced Materials Interfaces*, vol. 4, no. 24, Dec. 2017, doi: 10.1002/admi.201700737.

[12] Wolfgang Knoll and Rigoberto C. Advincula, *Functional Polymer Films*, vol. 1. Wiley, 2013.

[13] J. Torrance, P. Lacorre, C. Asavaroengchai, and R. Metzger, "Why are some oxides metallic, while most are insulating?," vol. 182, no. 6, 1991, doi: 10.1016/0921-4534(91)90534-6ï.

[14] "Free electron model," *Wikipedia*, 2022.

[15] V. O. Lum, D. B. Mcwhan, A. Menth, J. P. Remeika, % F Brinkman, and T. M. Rice, "PHYSICA L REVIEW B Metal-Insulator Transitions in Pure," 1973.

[16] V. I. Anisimov, J. Zaanen, and O. K. Andersen, "Band theory and Mott insulators: Hubbard U instead of Stoner I."

[17] "Hubbard model ," *Wikipedia*, 2022.

[18] Nevill Mott, *Metal-Insulator Transitions*, 1st ed. London: Taylor & Francis , 1990.

[19] J. Zaanen, G. A. Sawatzky, and J. W. Allen, "Band Gaps and Electronic Structure of Transition-Metal Compounds."

Chapter 2
Experimental Techniques

We discussed the synthesis techniques and characterizations used in our project in chapter 2. These techniques are classified in the following manner:

2.1 Sample Preparation

2.1.1 Bulk synthesis using solid-state reaction route

2.1.2 Thin film synthesis using PLD

2.2 Characterization techniques

2.2.1 X-ray Diffraction (XRD) technique

2.2.2 Raman Spectroscopy

2.2.3 Temperature-dependent resistivity measurement

2.1 Sample Preparation:

2.1.1 Bulk synthesis following solid-state reaction route:

In order to prepare bulk samples, solid state reaction is a widely utilized approach [1]. Here the reaction occurs in powder form, thus this is a solvent-free method. In this method, highly pure (about 99.99%) constituent powders were mixed in the appropriate stoichiometric ratio using high precision weighing mechine. The powder were ground using pestle-morter thoroughly for 3-4 hours and in order to ensure the homogeneous mixing of powders, we used propanol in between grinding procedure. As propanol is a volatile organic liquid, it evaporates gradually during grinding activity. It is also notable that the reaction of powder mixture doesn't initiate at room temperature. So, to initialize the reaction, we calcinated the powder mixture for several hours using box furnace. Meanwhile, some gases like CO_2, NO_2, and moisture were removed from the bulk sample. These grinding and calcination techniques were repeated again for uniform particle size and single phase formation of the sample. After third grinding, the powder sample was pressed in the form of pellet using the hydraulic press with a 20 mm die set under 4 tons of pressure for intimate contact of the sample. To

densify the pellet by removing air bubbles from it, the pellet was sintered in box furnace with a temperature that is higher than the calcination temperature. So the procedure can be summarized into the following points:

- Weighing and mixing the high purity powders in proper stoichiometric ratio
- Grinding the powder mixture to obtain larger surface area of contact among the reactants
- Calcination to initiate the reaction of the powder mixture
- Formation of pellet and sintering to densify the pellet

Synthesis of $NdNi_{1-x}Al_xO_3$ (x=0-0.2) targets:

We have prepared $NdNi_{1-x}Al_xO_3$ samples by mixing Nd_2O_3, NiO and Al_2O_3 powders with high purity (about 99.99% pure) in proper stoichiometric ratios. The reaction can be written in the following manner:

$$Nd_2O_3 + (1\text{-}x)\ NiO + \left(\frac{x}{2}\right) Al_2O_3 \longrightarrow NdNi_{1-x}Al_xO_3$$

The synthesis procedure of bulk sample is shown in the following block diagram:

Highly pure powders of Nd_2O_3, NiO and Al_2O_3 with required molar ratio were taken using high precision electronic weighing mechine

⬇

Proper grinding was done for 3-4 hours using pestle mortar for homogenous mixing and thereafter the powder mixture was calcinated at 800ºC for 12 hours in box furnace so that powder mixture reacts properly

⬇

To maintain uniform particle size, second grinding was done thoroughly for 2-3 hours and again calcination was done at 800ºC for 12 hours in box furnace to maintain uniformity and single phase

⬇

30 minutes grinding was done after second heating and finally using Hydraulic press, mixture was pressed in form of pellets (diameter = 20 mm) and then pellets were sintered at1000ºC in box furnace for 12 hours

2.1.2 Thin film synthesis using PLD:

Thin films have been widely employed for more than a half-century to make various devices such as electronic devices, instrument hard coatings, optical coatings, decorative parts, enzymatic glucose biosensors, neural circuits, and so on. The major steps followed to deposit thin films are given below:

- Production of ionic or molecular species
- Transport of that species to the substrate through a medium
- Condensation of the deposited film on the substrate via cooling or chemical or electrochemical reactions

We can easily classify the thin film deposition techniques into two categories:

a) Physical Vapour Deposition (PVD): Physical vapour deposition is a method for transferring atoms from a solid or molten source to a substrate via physical processes such as evaporation, sublimation, or ionic impingement on a target. The two most common PVD processes for depositing films are evaporation and sputtering.

b) Chemical Vapour Deposition (CVD): Chemical Vapour Deposition is used when the material deposited on the film is the result of a chemical reaction. It's commonly used in industry to make high-purity crystalline films of complex oxides, nitrites, and other compounds [2].

Our thin films were synthesized by Pulsed Laser Deposition (PLD) technology. It is the most widely used technology in the Physical Vapour Deposition (PVD) category.

Experimental design of PLD technique:

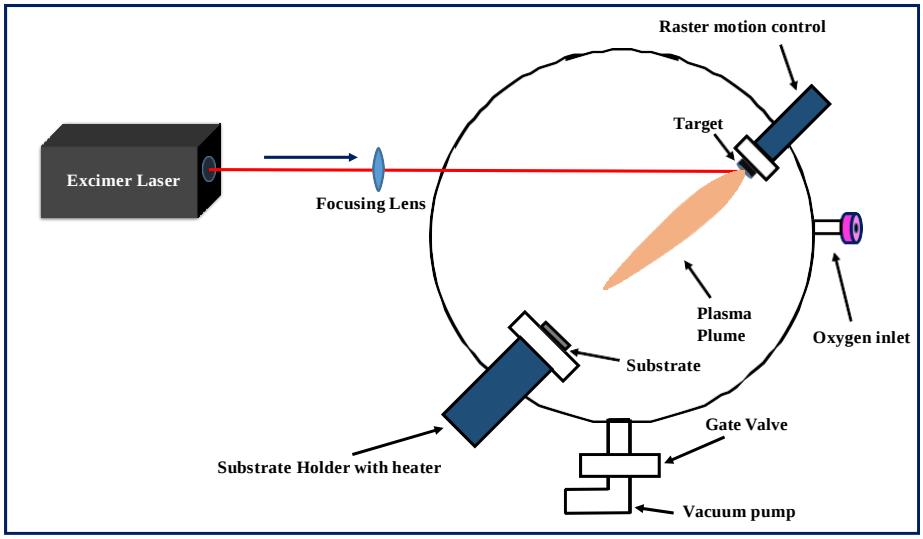

Figure 2.1: Schematic diagram of the pulsed laser deposition (PLD) system

PLD technique is one of the most efficient and versatile techniques to deposit thin films on suitable substrates. In this technique, we can use ultraviolet, visible, and infrared lasers. The most commonly used lasers are Q switched Nd:YAG excimer laser (λ - 1.064 μm, second harmonics – 532 nm, third harmonics 266 nm) which is also called solid-state laser, KrF (λ - 248nm), and ArF (λ - 193nm) excimer lasers, etc. Among these varieties of lasers, we used KrF excimer laser which emits ultraviolet pulses for our PLD chamber. The PLD chamber, which is made of stainless steel, consists of target holder, substrate holder, heating instrument, and process gas inlet. In order to ablate the ions uniformly from the target, the raster and rotational motion of the target holder are well programmed into the PLD chamber. The substrate holder is attached to the target holder at a certain distance. During thin film deposition, the substrate holder is connected to a heater to maintain the requisite deposition temperature. A rotary pump and a turbomolecular

pump are used in the vacuum system. The rotary pump reduces the ambient pressure in the PLD chamber to roughly 10^{-3} Pa. The turbo-molecular pump can achieve base pressure of ~10^{-6} Pa. Figure 2.1 and **2.2** represent the schematic diagram and experimental set-up of PLD chamber, respectively.

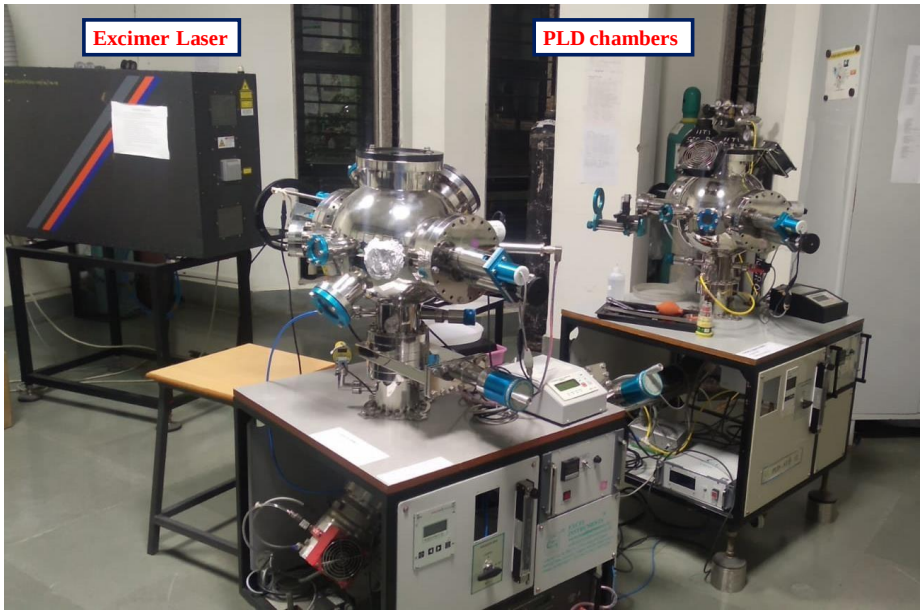

Figure 2.2: Image of experimental setup of PLD system at the thin film laboratory, IIT Indore

When a high-energy laser beam strikes the material at a vacuum and temperature, plasma plume emerge [3]. Many review publications provide theoretical explanations for the formation of plasma plume [4],[5]. Plasma plume ablation cannot be explained by a single mechanism, according to studies, but rather by a combination of mechanisms. Ablation occurs when the absorbed laser energy E_{ab} is larger than the binding energy E_b of the atoms on the target materials' surface. The following is a representation of the condition: $E_{ab} > E_b$. When a laser pulse is absorbed by the target, the energy is transformed first into electronic excitation, then into thermal, chemical, and mechanical energy, causing evaporation, ablation, and plasma production. The laser ablation and absorption process take about 30

nanoseconds. Plasma plume made up of the ablated ions and materials take an elliptical or roughly circular shape and are directed towards the substrate. Adjusting the partial pressure of the inlet gas can change the shape and focus of the plasma plume and also balances the oxygen stoichiometry of the depositing sample. The kinetic energy and scattering rate of the plasma plume can be adjusted by partial pressure, and hence this deposition parameter can be regulated for optimal growth. In general, the kinetic energy of ions in the plasma plume ranges from 0.1 eV to 10 eV.

Thin film growth types:

The growth of certain materials on the particular substrates can occur in several manners after the nucleation. We can describe majorly the growth type by the following three models (Figure 2.3):

1. **Volmer-Weber growth model:**

   It happens when the tiniest stable clusters form on the substrate and expand into three-dimensional islands. The atoms or molecules being deposited are more tightly linked to each other than to the substrate material in this growth model. This is common when the film and substrate are made of different materials. When metal and semiconductor (i.e., Group IV, III–V, etc.) films are formed on oxide substrates, this growth model is commonly observed [6].

2. **Frank-van der Merwe growth model:**

   This process, often known as the layer-by-layer model, is based on the epitaxial growth of films on the crystal surface. This kind of growth is two-dimensional (2D). The atoms of thin films are strongly connected to the substrate in this mode, and each layer is gradually less strongly bonded than the one before it. The atoms are deposited in a monolayer on the substrate's surface. This model explains the growth of epitaxial and smooth thin films. Epitaxial growth of semiconductors and oxide materials is a good illustration of this [7].

3. **Stranski-Krastanov growth model:**

It's a mix of layer-by-layer growth and island growth model. This model is known as 'layer-plus-island growth,' and it is the combination of the two-dimensional and three-dimensional growth models. In this growth phase, following the layer-by-layer formation of one or more monolayers, further layer-by-layer growth becomes energetically unfavorable, and islands arise. This type of growth has been seen in a variety of metal-metal and metal-semiconductor systems.

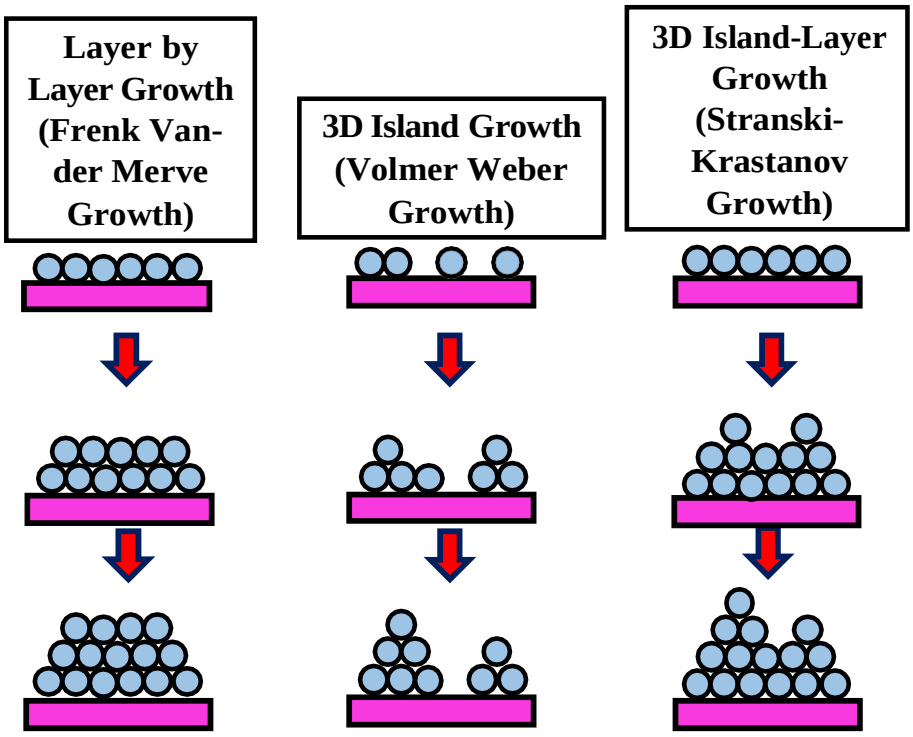

Figure 2.3: Schematic of different growth models of thin film on the substrate

Parameters of thin film growth:

The phase stabilization, quality, and epitaxial nature of the thin film are all influenced by a number of external factors given below [8]:

- **Laser energy:** Controls the kinetic energy of the ions ablated from the target and growth rate on the substrate.

- **Process gas partial pressure:** Controls the plume shape and maintains the proper stoichiometric ratio, especially in complex oxides.
- **Substrate temperature:** Optimum substrate temperature helps in nucleation and growth procedure.
- **Target to substrate distance:** Maintains the angular spread of the plasma plume.

Substrate selection:

Thin films are deposited on the substrate. Therefore, substrate selection plays a crucial role in thin film synthesis. We have selected $LaAlO_3$ (LAO) single crystal substrate with (001) orientation in our case. In order to get an idea about strain experienced by thin films, we can look at the pseudo-cubic lattice parameters of $NdNiO_3$ bulk and LAO (001) substrate. After calculating the lattice mismatch, we have obtained that the film experiences the in-plane compressive strain and therefore, the out-of-plane tensile strain.

Synthesis of $NdNi_{1-x}Al_xO_3$ (x=0-0.2) thin films on LAO (001) substrate:

$NdNi_{1-x}Al_xO_3$ (x=0-0.2) thin-film depositions are carried out on a single crystal $LaAlO_3$ (LAO) substrate with dimensions of ($2 \times 5 \times 0.5$) mm. The substrates were properly sonicated for 10 minutes, first in acetone and subsequently in propanol. Before deposition, the chamber was evacuated, and then filled with pure oxygen as background gas.

During the deposition, the following parameters were maintained:

Table-1

Parameter	Value
Laser Ablation Energy	310mJ
Laser Wavelength	248 nm
Target to Substrate Distance	4.5 cm
Base Pressure	1.1×10^{-3} Pa

Oxygen Partial Pressure	40 Pa
Deposition Temperature	720℃
Repetition Rate	4 Hz
No. of shots	1400

After deposition, the deposited thin films were post-annealed at 720 ℃ keeping 1000 Pa oxygen partial pressure for 3 minutes.

Advantages of PLD:

1) It allows for more customization of laser parameters such as laser energy, substrate temperature, target to substrate distance, order of vacuum, oxygen partial pressure, and others.
2) PLD maintains phase purity of thin films even when the target is multiphase [9].
3) Regulating the number of pulses controls the thickness of the sample.
4) PLD may also be used to make multilayer films and heterostructures.
5) In PLD, the stoichiometry of the film is controlled by the ability to construct a target with the required composition, as compared to techniques like Molecular beam epitaxy (MBE), where the composition is controlled by adjusting the ratio of the various sources arriving on the substrate.

Disadvantages of PLD:

1) As the plume size in PLD is narrow enough, it is very difficult to deposit thin films with uniform thickness.
2) During the fast heating and cooling process, particulates such like micro size lumps or droplets are formed in the target.

2.2 Characterization Technique:

The X-ray diffraction (XRD) method has been used to investigate the phase purity of all thin films once they are synthesized.

Room temperature and temperature-dependent Raman spectroscopy are used to investigate any structural changes that occur as a result of changing any parameter, such as temperature or doping percentages. The closed-cycle refrigerator (CCR) is used to measure the temperature-dependent resistivity of thin films over a wide temperature range of 300K to 12K.

Each characterization technique's specifics are explained in the sections below.

2.2.1 X-ray Diffraction (XRD) technique:

X-ray diffraction is one of the most extensively used techniques for the characterization of samples to extract information on the atomic scale for both crystalline and non-crystalline materials, because the wavelength of X-ray, which is of the order of Å, is equivalent to interatomic distances. When an X-ray strikes a material, it is diffracted by different sets of atomic planes in the crystal structure, and if d-spacing (the spacing between the planes) and the angle of incidence with respect to the plane satisfy the Bragg relation $2d\sin\theta = n\lambda$, where d is the inter-planer distance, n is an integer, and θ is the half of the angle between the incident and diffracted rays, then constructive interference between the diffracted waves occurs. If we consider n = 1/2, 3/2, and so on, then the diffracted waves result in destructive interference. In 1912, Max von Laue and W. L. Bragg and his father W. H. Bragg discovered this technique which opened a new era of material characterization [10]. This approach is commonly used to investigate the materials' internal structure, lattice crystallinity, lattice parameters, strain on the lattice, *etc* [11].

Working Principle:

To begin, an alternating voltage is applied between two electrodes to heat the filament inside the cathode tube. As the filament heats up, free electrons travel faster from the cathode to the anode and eventually impact the anode surface, resulting in the generation of X-

rays in the X-ray tube. The X-rays that come from the tube strike the sample's surface. As the wavelength of these originating X-rays has a wavelength of the order of the lattice parameter, the diffraction of X-rays occurs with continual change in intensity adopting different incident angles.

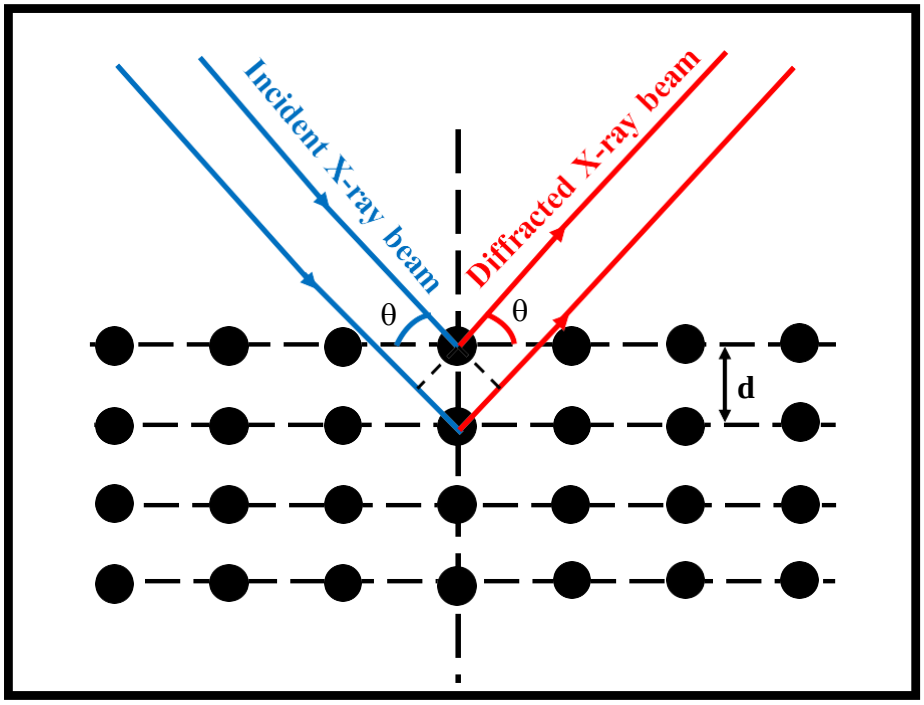

Figure 2.4: X-ray diffraction through Bragg's reflection in the atomic planes

The concept of X-ray diffraction is totally based on the condition of Bragg's law (Figure 2.4). If we take two parallel X-ray beams falling on two consecutive atomic planes, then the path difference between the two beam paths becomes $2d\sin\theta$. The constructive and destructive interferences happen in two different situations of the following condition, called Bragg's law.

$$2d\sin\theta = n\lambda \text{ -------- } (2.1)$$

The constructive interference occurs if the path difference is equal to the integer number of the X-ray wavelength. Similarly, in the

case of the path difference equal to half of the odd integers, the interference is destructive.

In the schematic of XRD shown in figure 2.5, 2θ represents the angle between the incident and diffracted rays, ϕ is the angle of rotation about the direction of the surface, χ is the angle of rotation about the line parallel to the surface, ω is the angle of rotation about the axis perpendicular to the lines perpendicular and parallel to the surface.

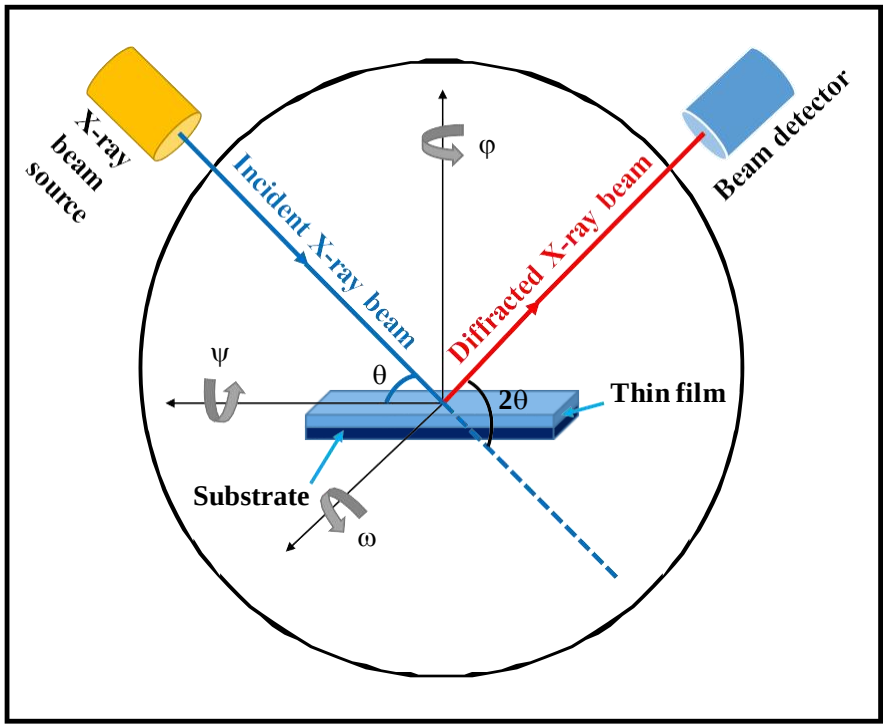

Figure 2.5: Schematic diagram of XRD setup showing different angles of rotation

In the case of film deposited on the substrate, the film experiences two types of strain due to lattice mismatch. Depending upon the sign of lattice mismatch, i.e. simply the lattice parameters of the film and substrate, we can divide the strains into two types:

A. Tensile strain:

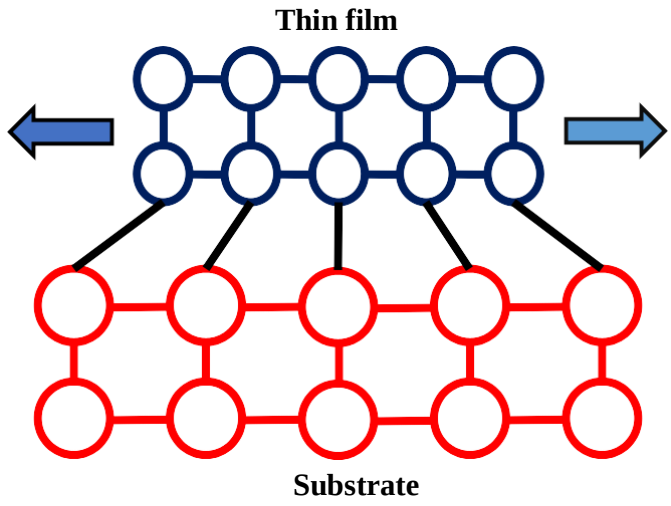

Figure 2.6: Thin film showing tensile strain on the substrate

In tensile strain (Figure 2.6), the lattice parameter of the thin film is less than that of the substrate. So, the film tries to expand itself resulting in the decrease of the out-of-plane lattice parameter, and hence to satisfy Bragg's law, the shifting of diffraction angle in the XRD pattern towards higher value becomes the signature of tensile strain in the film owing to the substrate.

B. Compressive strain:

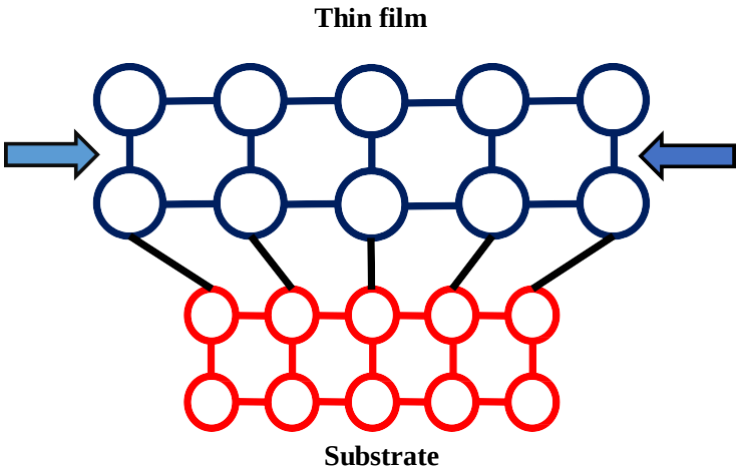

Figure 2.7: Thin film showing compressive strain on the substrate

In compressive strain (Figure 2.7), the lattice parameter of the thin film is more than that of the substrate. So, the film tries to compress itself resulting in the increase of the out-of-plane lattice parameter, and hence to satisfy Bragg's law, the shifting of diffraction angle in the XRD pattern towards lower value becomes the signature of compressive strain in the film owing to the substrate.

2.2.2 Raman Technique:

When a monochromatic light or light with a very narrow frequency range is incident on a medium, the frequency of scattered light may be the same of the incident ray. Moreover, the frequency and its corresponding energy of the scattered light may be above or below of the incident light.

If the scattered radiation possesses almost entirely the energy of incident radiation, the scattering is called Rayleigh scattering. In addition, if the scattered radiation achieves discrete frequencies above and below the incident radiation frequency, the scattering is called Raman scattering as this phenomenon was discovered by C. V. Raman and K. S. Krishnan in 1928 [12]. As the invention of Raman spectroscopy opened a new path of progress in new generation science, A. V. Raman was awarded Nobel Prize in 1930 [13].

The quantum theory of the Raman effect:

In the quantum theory of the Raman effect, we deal with the collision of photons having a frequency ν with molecules in the sample. These collisions may be elastic and inelastic. The photons will be deflected in the same way without losing any energy if the collision is perfectly elastic. During an inelastic collision, however, energy may be exchanged between photon and molecule. Only the quantal laws allow the molecule to gain or lose energy; that is, its energy change, ΔE joules, must be the difference in energy between two of its permissible states. A change in the molecule's vibrational and/or rotational energy must be

represented by ΔE. The photon will be dispersed with energy hν - ΔE and the corresponding radiation will have a frequency ν - ΔE/h if the molecule gains energy ΔE. Similarly, the scattered frequency will be ν + ΔE/h if the molecule loses energy ΔE [14] (Figure 2.8).

Thus, the scattered radiation with ν - ΔE/h frequency is called Stokes' radiation and the higher frequency radiation is called anti-Stokes' radiation. As the population of lower energy states is higher than higher-order energy states and also, the Stokes' radiation and anti-Stokes' radiation are seen due to the transition of lower to higher and higher to lower energy states in the molecules, respectively, the intensity of Stokes' radiation is generally higher than that of anti-Stokes' radiation.

The classical theory of the Raman effect:

The Raman effect's classical theory leads to a knowledge of a fundamental notion in the form of spectroscopy: a molecule's polarizability. When a molecule is exposed to a static electric field, the positively charged nuclei are drawn to the negative pole of the field, while the electrons are drawn to the positive pole. The molecule is considered to be polarised because of the separation of charge centers, which generates an induced electric dipole moment in the molecule. The value of the induced dipole, μ, is determined by the amount of the applied field, E, as well as the molecule's ability to be distorted. We can write the following expression:

$$\mu = \alpha E \text{--------} (2.2)$$

where α is known as the polarizability of the molecule.

When a sample of these molecules is exposed to a beam of radiation with a frequency of ν, the electric field experienced by each molecule fluctuates as shown in the following equation:

$$E = E_0 \sin 2\pi\nu t \qquad (2.3)$$

Thus, the induced dipole moment also undergoes the oscillation of frequency ν by the following expression:

$$\mu = \alpha E = \alpha\, E_0 \sin 2\pi\nu t \text{--------} (2.4)$$

As an oscillating dipole emits radiation of its own oscillating frequency, the frequency of incident and scattered radiation is equal. This is the classical explanation of Rayleigh scattering.

In addition, due to some internal motions such as rotation and vibration, the polarizability changes periodically. If we consider only the vibrational motion with frequency ν_{vib} which changes the polarizability of the molecule, then the induced dipole moment will be:

$$\mu = \alpha E = (\alpha_0 + \beta \sin 2\pi\nu_{vib} t)\, E_0 \sin 2\pi\nu t \text{ --------} (2.5)$$

which corresponds the following expression (using trigonometric formula):

$$\mu = \alpha_0 E_0 \sin 2\pi\nu t + \frac{1}{2}\beta E_0 \{\cos 2\pi(\nu - \nu_{vib})t - \cos 2\pi(\nu + \nu_{vib})t\} \text{---------} (2.6)$$

The first term in equation (2.6) has the frequency same as the frequency of incident radiation which corresponds to the Rayleigh scattering phenomena. In the second and third terms, two frequencies arise: one has a frequency less than the incident beam frequency and another has a greater one. Therefore, the term having (ν - ν_{vib}) frequency arises due to Stokes' radiation and another one (having (ν + ν_{vib}) frequency) arises due to anti-Stokes' radiation (Figure 2.9).

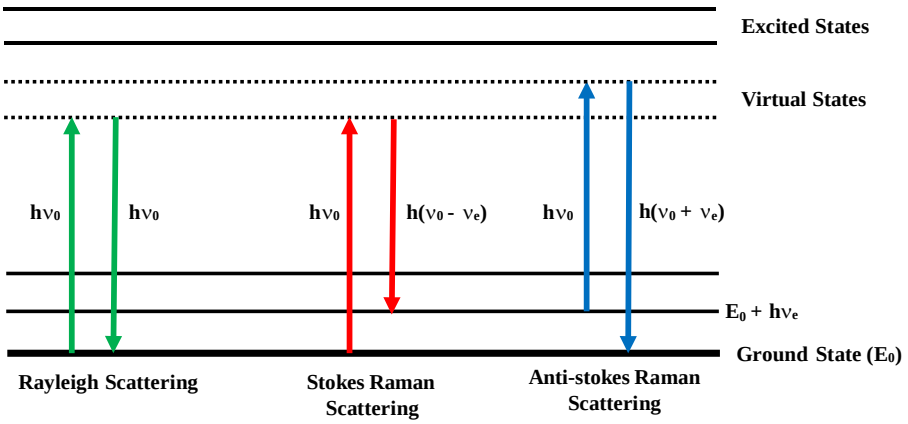

Figure 2.8: Schematic of energy level diagram showing various types of emissions

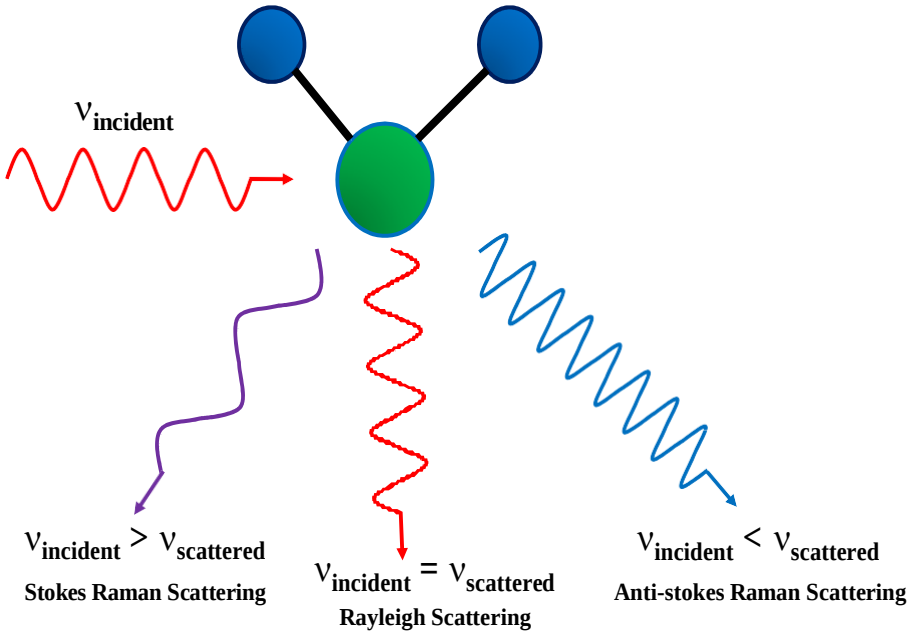

Figure 2.9: Schematic representation of interaction of laser light with a molecule and its consequence

Instrumentation for Raman spectroscopy:

The components in Raman spectroscopy consist of (Figure 2.10):

- Laser
- Beam splitter
- Microscope
- Heater
- Liquid N_2-supply
- Temperature controller
- CCD (charge-coupled device) and recording systems
- Filters

In our case study, the Horiba LabRam micro-Raman Spectrometer was used to explore phonon modes at room temperature using a He-Ne laser with a wavelength of 632.8 nm.

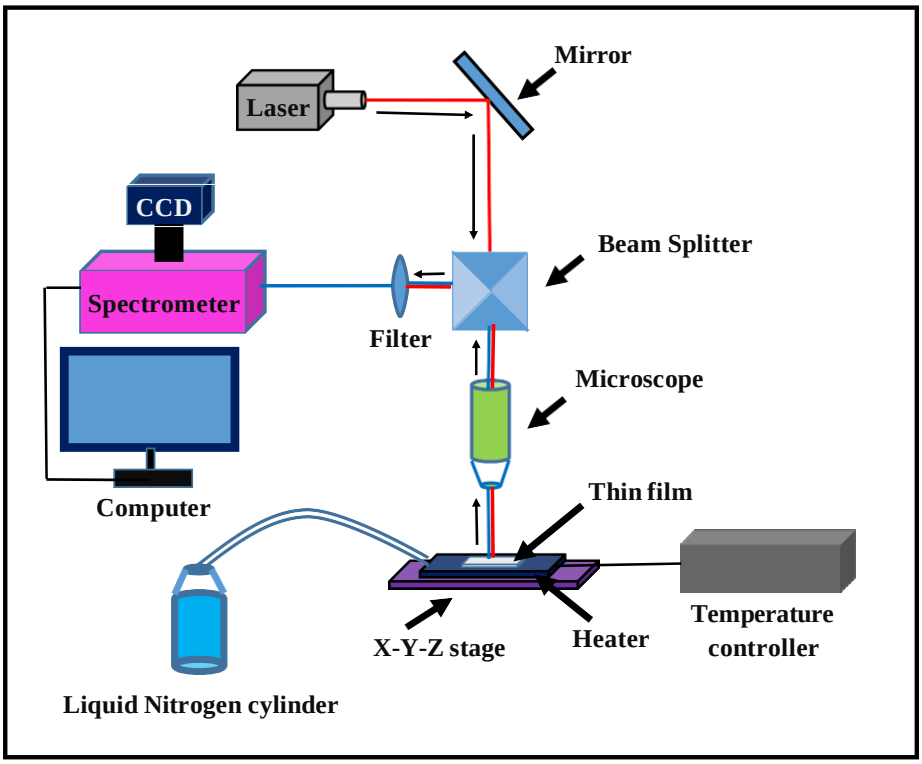

Figure 2.10: Schematic of micro-Raman spectroscopy setup

Advantages:

As the diameter of the laser beam used in the Raman study is small, we can easily investigate Raman spectra using the small area of the sample.

Disadvantage:

The laser light source used in Raman spectroscopy is the reason behind local heating as well as the thermal decomposition of the sample. This is one of the main drawbacks of studying Raman spectroscopy of any particular sample.

2.2.3. Temperature-dependent resistivity measurement:

The resistivity of a material is defined as the resistance generated by a blockage in the flow of charge carriers in a lattice. Resistivity measurements allow for the determination of a material's unique electrical properties when subjected to external perturbations.

Temperature, for example, has a considerable impact on the resistivity of metals and insulators. The resistivity of metals increases as the temperature rises, but the resistivity of insulating materials decreases as the temperature rises. As a result, resistivity measurements become a useful tool for studying structural phase shifts in metal-insulator systems that are accompanied by electronic transitions. The resistivity of a sample can be calculated by:

$$\rho = R\frac{A}{l} \quad \text{----- (2.7)}$$

where R is the resistance of the sample keeping the shortest distance of the probes in measurement system l and cross-section area A. This R-value can be calculated by Ohm's law: $R = \frac{V}{I}$, where V is the potential difference of the probes at a particular current I. There are two methods for measuring electrical resistivity (ρ): the two-probe method and the four-point probe method. For extremely resistive samples, the two-probe approach is appropriate. The four-probe approach, on the other hand, is best for conducting samples with low resistance.

Four-probe method:

The four-probe method is one of the mostly-used and versatile techniques to measure the resistivity of the sample due to its accuracy in measurement. Thus, it's best for low-resistive samples. The use of separate probes for the source and measurement eliminates contact resistance, making this approach superior to the two-probe method.

To assess the resistance of a single crystal or a thin film, four probe approaches can be utilized. Current flows via the outer contacts, which are near the sample's edges, and the potential difference between the inner contacts is measured [15] (Figure 2.11). Furthermore, this approach may be used when the distance between the probes is minimal in comparison to the sample's smaller dimension.

Therefore, it provides a number of benefits over the two-probe approach:

I. It eliminates contact resistances, which can lead to measurement errors.

II. When the sample resistance is low and thus, the contact resistance may influence the value, this method is incredibly beneficial [16].

III. Because we're taking the difference of the voltage and current across two probes, there's less chance of error in the data.

The four-probe approach was used to measure the resistivity of $RNiO_3$ thin films. The samples are typically in the shape of a long, thin rectangular bar measuring 5×2 mm in dimension. Four collinear connections were created on the surface of the thin film with Epoxy technology's conductive silver paste (EPO-TEK EE 129-4), and the samples were heated for 10-15 minutes before being placed in the measurement chamber.

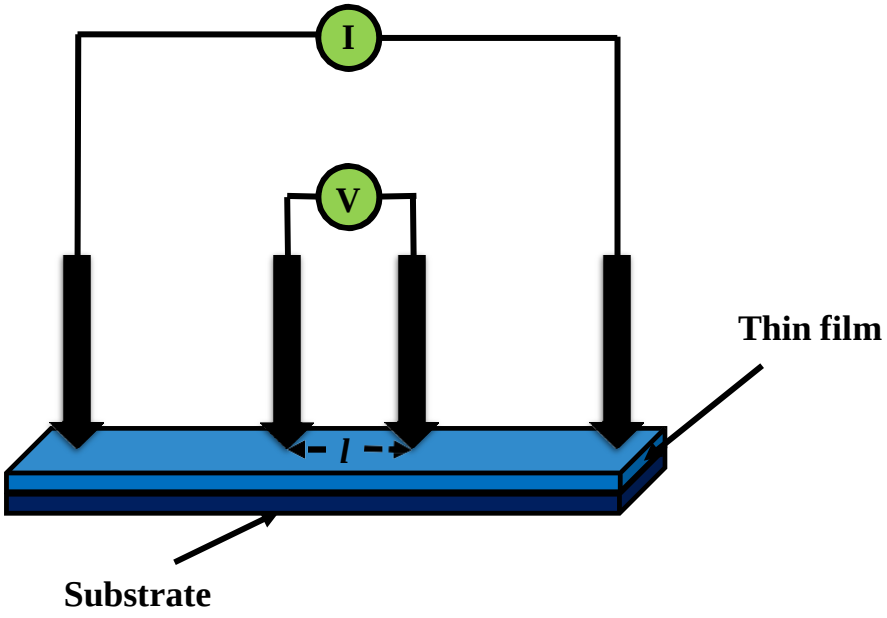

Figure 2.11: Four probe setup

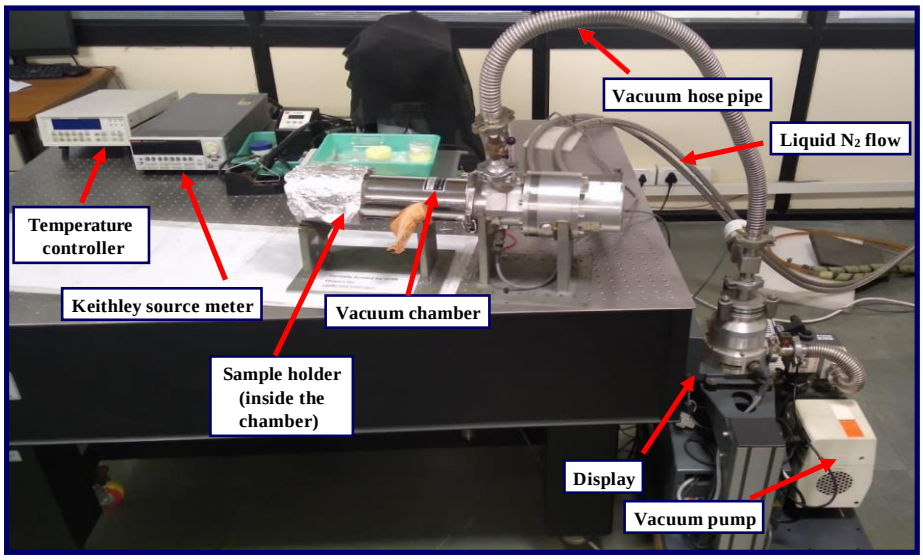

Figure 2.12: Image of the temperature-dependent resistivity measurement setup at thin film laboratory in IIT Indore

In our project work, a JANIS RESEARCH CCR cryostat was used to assess temperature dependent resistivity of the samples. The system can detect the resistivity of two samples at the same time, which is useful for a comparative examination of two samples. A temperature controller produced by LakeShore was used to monitor and control the temperature. The voltage was measured by providing a certain amount of current using the KEITHLEY-2612 A Source-Meter. Following the achievement of a good vacuum, measurements were made using the LABVIEW RT-5d in the temperature range of 300K-12K. Image of the experimental setup for temperature-dependent resistivity measurements is shown in figure 2.12.

References:

[1] A. Venimadhav, I. Chaitanya Lekshmi, and M. Hegde, “Strain-induced metallic behavior in $PrNiO_3$ epitaxial thin ®lms.”

[2] Wolfgang Knoll and Rigoberto C. Advincula, *Functional Polymer Films*, vol. 1. Wiley, 2013.

[3] K. Wang, G. Tai, K. H. Wong, S. P. Lau, and W. Guo, “Ni induced few-layer graphene growth at low temperature by pulsed laser deposition,” *AIP Advances*, vol. 1, no. 2, 2011, doi: 10.1063/1.3602855.

[4] F. L. Forgerini and R. Marchiori, “A brief review of mathematical models of thin film growth and surfaces. A possible route to avoid defects in stents,” *Biomatter*, vol. 4. p. e28871, 2014. doi: 10.4161/biom.28871.

[5] M. Henini, *Handbook of Thin-Film Deposition Processes and Techniques*, *Microelectron* . 2003.

[6] Anthony R. West, *Solid State Chemistry and its Applications*, 2nd ed. Wiley, 2014.

[7] Frank F C and van der Merwe J H, “One-Dimensional Dislocations. II. Misfitting Monolayers and Oriented Overgrowth,” *Proc. R. Soc. Lond. Ser. A* , vol. 198, pp. 216–225, 1949.

[8] H.-U. Krebs *et al.*, “Pulsed Laser Deposition (PLD)-A Versatile Thin Film Technique.” [Online]. Available: http://www.gwdg.de/~upmp

[9] “Titanium nitride,” *Wikipedia*, 2022.

[10] Douglas B. Chrisey and Graham K. Hubler, *Pulsed Laser Deposition of Thin Films*. Wiley–Blackwell, 1994.

[11] “ Pulsed Laser Deposition,” *Wikipedia*, 2022.

[12] D. A. Long, “Introductory Raman Spectroscopy. John R. Ferraro, Kazuo Nakamoto and Chris W. Brown. Academic Press, Amsterdam, Second Edition, 2003. xiii + 434,” *Journal of Raman Spectroscopy*, vol. 36, no. 10, pp. 1012–1012, Oct. 2005, doi: 10.1002/jrs.1407.

[13] “C. V. Raman,” *Britannica*.

[14] C. N. Banwell, A. Elaine, and M. Mccash, “FUNDAMENTALS OF MOLECULAR SPECTROSCOPY FOURTH EDITION.”

[15] G. Catalan, “Progress in perovskite nickelate research,” *Phase Transitions*, vol. 81, no. 7–8. pp. 729–749, Jul. 2008. doi: 10.1080/01411590801992463.

[16] “Resistivity by Four Probe Method (Theory) : Solid State Physics,” *Virtual Lab : Physical Sciences :* Amrita Vishwa Vidyapeetham Virtual Lab.

Chapter 3
Results and Discussions

We have successfully synthesized Al-doped $NdNiO_3$ targets using solid-state reaction method. As the ionic radius of Al is nearer to the ionic radius of Ni, Ni-ion will be substituted by Al-ion in $NdNiO_3$. We have kept the doping percentage as 0 %, 2 %, 5 %, 10 %, and 20 %. The thin films of all doped samples were deposited on $LaAlO_3$ (LAO) single crystal substrates keeping 20 nm thickness using PLD technique. The properties of prepared thin films were studied by performing XRD, Raman, and temperature-dependent resistivity measurement as described elaborately in chapter-2. The experimental data gives us the clarity on the characteristics of the films vividly.

3.1 X-ray diffraction:

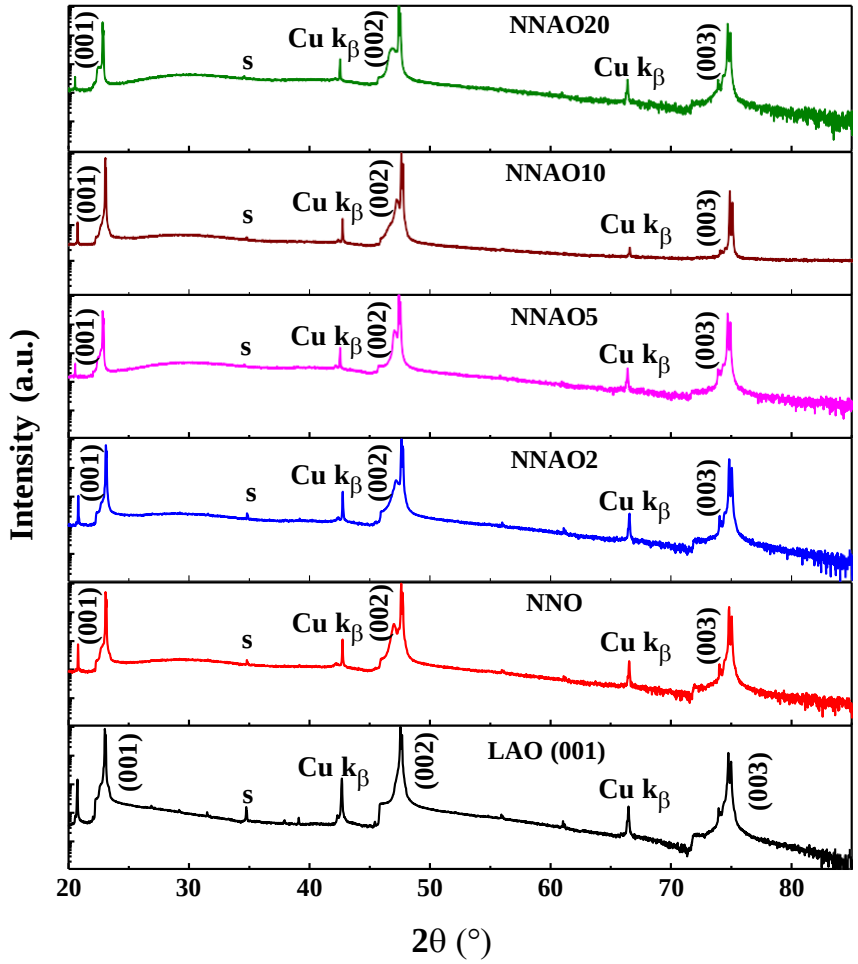

Figure 3.1: Full scale XRD Patterns of $NdNi_{1-x}Al_xO_3$ (x= 0- 0.2) films on LAO (001) substrate

The phase purity and out-of-plane lattice parameter were checked using X-ray diffraction (XRD) measurement on a Bruker D8 Advance X-ray diffractometer (Cu K_α). No undesired peak is observed in the XRD patterns of the films, as illustrated in Figure 3.1, which confirms that the films are grown highly oriented growth without any impure phase. This implies that the phase purity and structure of $NdNiO_3$ films are preserved even after 20% Al doping. The lattice mismatch calculation can be obtained from the following mathematical expression:

$$\text{Lattice Mismatch (\%)} = \frac{a_{sub} - a_{film}}{a_{film}} \times 100,$$

where a_{sub} and a_{film} are the pseudocubic lattice parameters of the substrate and thin film, respectively.

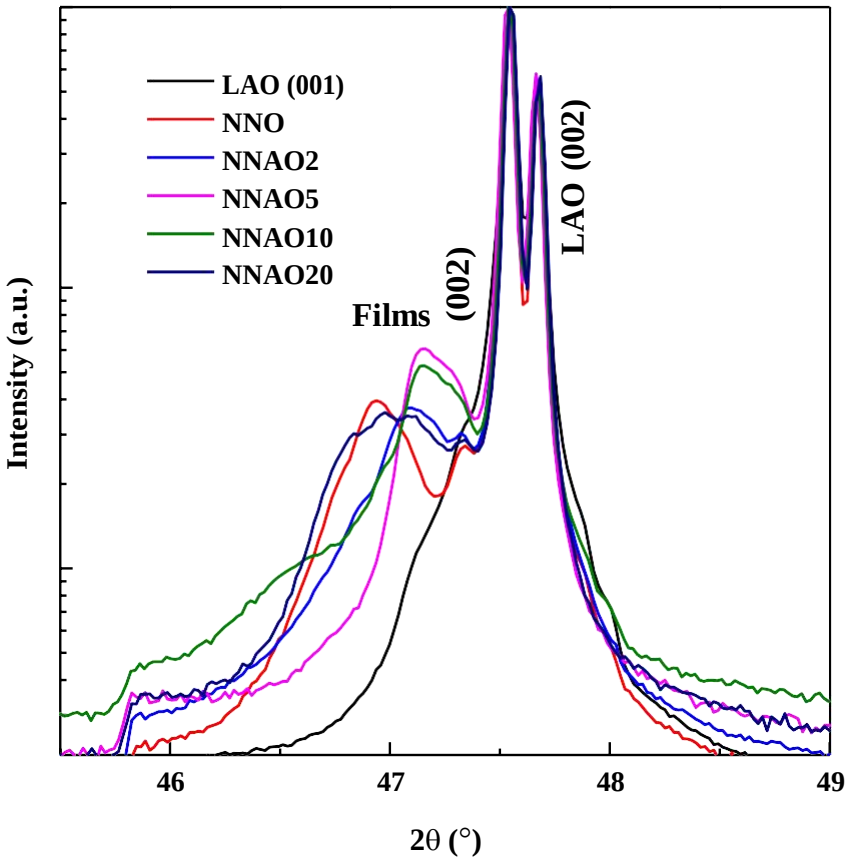

Figure 3.2: Magnified view of the (002) peak of XRD patterns of $NdNi_{1-x}Al_xO_3$ films (x= 0- 0.2) on LAO (001) substrate

The pseudocubic lattice parameter of bulk $NdNiO_3$ is 3.807 Å, while that of LAO is 3.79 Å. Based on these parameters, the lattice mismatch comes out to be ~ -0.44%. The negative value of lattice mismatch confirms that $NdNiO_3$ thin film experiences an in-plane compressive strain and, therefore, it corresponds to the out-of-plane tensile strain. The out-of-plane parameter (c) of the $NdNiO_3$ thin film formed on the LAO (001) substrate, derived from the (002) peak of the X-ray diffraction pattern, is 3.86 Å. The out-of-plane parameter of the $NdNiO_3$ thin film is greater than the value of pseudocubic lattice parameters (a_{pc} = 3.807 Å) of polycrystalline $NdNiO_3$ solid, indicating that the film has out-of-plane tensile strain. From figure-3.2, a systematic broadening of the (002) peak is also visible with increasing doping percentage in these XRD patterns of NNAO/LAO films. This broadening implies the increment of disorder with increasing doping percentage. Table-2 shows the FWHM values of the (002) peaks as well as out-of-plane lattice parameters (c-parameters) of thin films.

Table-2

Sample	2θ (°)	c-parameter (Å)	FWHM (°)
$NdNiO_3$	47.02	3.86	0.25
$NdNi_{0.98}Al_{0.02}O_3$	47.20	3.85	0.25
$NdNi_{0.95}Al_{0.05}O_3$	47.07	3.86	0.27
$NdNi_{0.90}Al_{0.10}O_3$	47.26	3.84	0.27
$NdNi_{0.80}Al_{0.20}O_3$	46.88	3.87	0.46

3.2 Temperature-dependent resistivity measurement:

Figure 3.3 depicts the temperature-dependent resistivity measurements performed on all $NdNiO_3$ thin films. The increase in doping percentage leads the metal-to-insulator transition (T_{MI}) to shift

to a higher temperature, which correlates to the insulating phase exhibiting in a wide temperature range. In the temperature range studied, there is no evidence of a phase transition in the 20% doped NNO film (12 - 300 K). The T_{MI} is determined by determining the temperature at which the resistivity curve's slope changes. The temperature coefficient of resistivity (α) can be generally defined as the amount of change in resistivity with a particular temperature change. As a result, when the transition happens, α alters its sign. This metal to insulator transition happens at roughly 75 K in the undoped film. The doped samples with x=0.02, 0.05, and 0.10 have T_{MI}s of around 135 K, 150 K, and 160 K, respectively. Except for $NdNi_{0.8}Al_{0.2}O_3$, which shows a negative value of α in this temperature range, the temperature coefficient of resistivity has a positive value for other samples at higher temperatures in metallic states, as shown in figure-3.4. As a result, in the case of $NdNi_{0.8}Al_{0.2}O_3$ film, no transition in the resistivity data and the negative value of α confirms the insulating phase throughout a wide temperature range. The low-temperature region of the 5% doped sample shows a clear hysteresis loop, indicating a first-order phase transition with the coexistence of metallic and insulating phases.

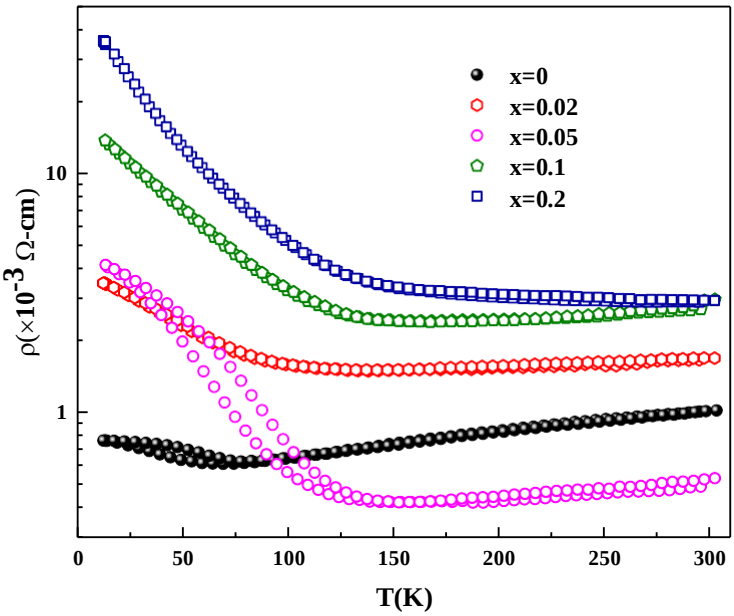

Figure 3.3: Resistivity vs Temperature behavior of $NdNi_{1-x}Al_xO_3$ (x= 0- 0.2) thin films grown on LAO (01) Substrate

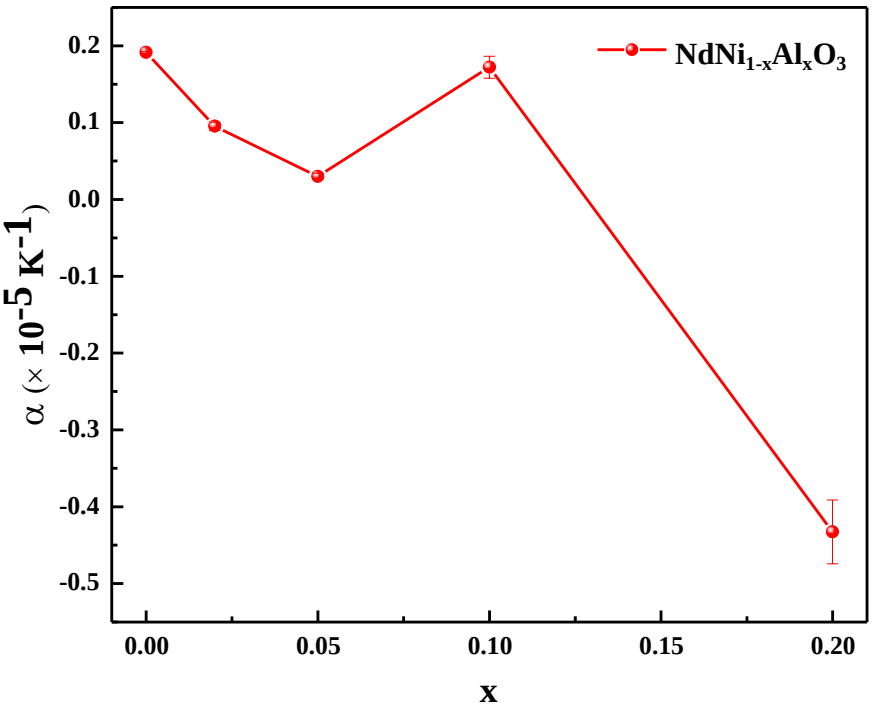

Figure 3.4: Coefficient of resistivity vs Doping percentage of $NdNi_{1-x}Al_xO_3$ (x= 0- 0.2) thin films grown on LAO (001) Substrate

3.3 Raman Spectroscopy:

Raman spectroscopy is now a very effective and adaptable tool for investigating the structural properties and phonon modes of nickelate thin films. It is susceptible to any change in the local geometry. So, to elucidate the doping-dependent structural properties of $NdNiO_3$ thin films, room temperature Raman spectra have been recorded. According to crystal symmetry analysis, $NdNiO_3$ shows $GdFeO_3$-type orthorhombically distorted structures belonging to the *Pbnm* space group at ambient temperatures. This structural distortion occurs due to the anti-phase tilting of adjacent NiO_6 octahedra ($a^-a^-c^+$ in Glazer's notation). In the polycrystalline bulk form, the primitive unit cell contains 20 ions with 60 vibrational modes ($7A_{1g} + 7B_{1g} + 5B_{2g} + 5B_{3g} + 8A_u + 8B_{1u} + 10B_{2u} + 10B_{3u}$) exhibiting at the centre of Brillouin zone. Out of these modes, 24 Raman modes ($7A_{1g} + 7B_{1g} + 5B_{2g} + 5B_{3g}$) have been identified.

From room temperature Raman spectra, we can observe 7 Raman modes (A_g + $3B_{1g}$ + $2B_{2g}$ + B_{3g}) for $NdNi_{1-x}Al_xO_3$ thin films keeping LAO (001) substrate as background in the spectral range 100-1000 cm^{-1} (Figure-3.5). The absence of other Raman modes can be attributed to highly orientated planes in thin films. The B_{2g} mode at 427 cm^{-1} appears due to the tilting of NiO_6 octahedra and, consequently, the change in Ni-O-Ni bond angle [1]. From the figure-3.6, it is clear that the values of full-width half maxima (FWHM) of this mode increase with the increment of doping percentages. This broadening of the peaks with doping is indicative of structural disorder in thin films. Furthermore, from this figure (Figure-3.6), we can easily observe the blue shifting of this mode with increasing doping fraction. This is the signature of the increment of octahedral tilting with increasing the doping fraction. The FWHM and peak position variations of this B_{2g} mode are tabulated in table 3, concerning Al-doping percentages of $NdNiO_3$ thin films.

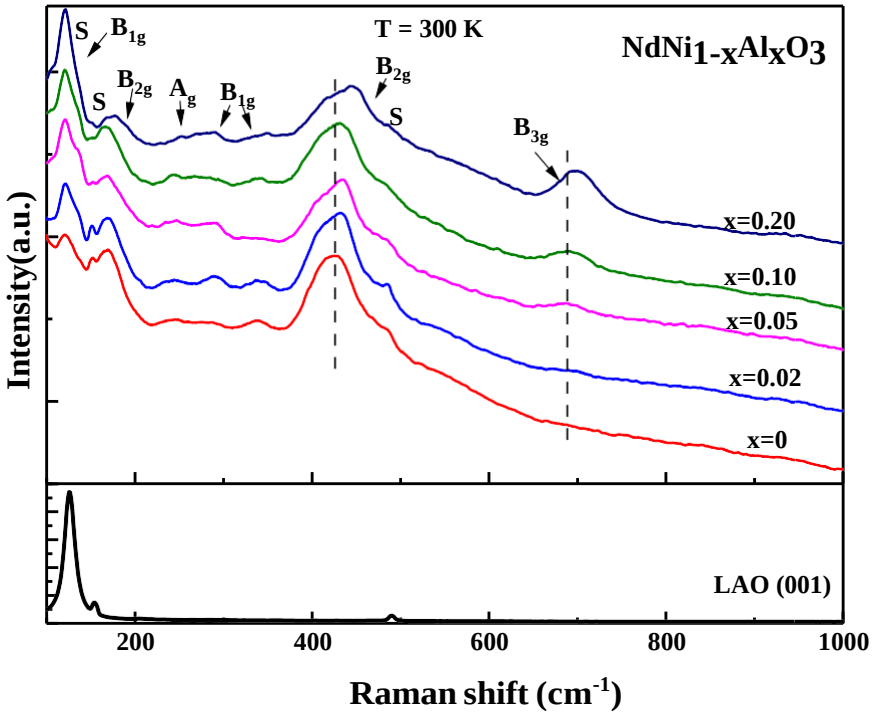

Figure 3.5: Room temperature Raman spectra of $NdNi_{1-x}Al_xO_3$ (x = 0 - 0.2) thin films grown on LAO (001) substrate

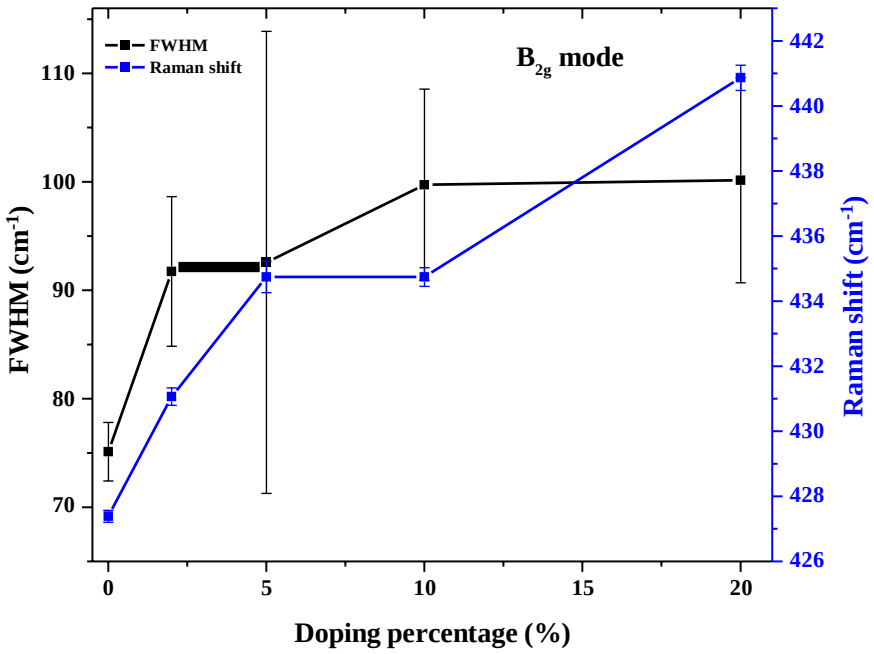

Figure 3.6: The variation of FWHM and Raman shift of B_{2g} mode at 427 cm^{-1} with doping percentages

Table-3

Sample	FWHM (cm^{-1})	Peak Position (cm^{-1})
$NdNiO_3$	75.10	427.39
$NdNi_{0.98}Al_{0.02}O_3$	91.72	431.06
$NdNi_{0.95}Al_{0.05}O_3$	92.56	434.74
$NdNi_{0.90}Al_{0.10}O_3$	99.73	436.16
$NdNi_{0.80}Al_{0.20}O_3$	100.14	440.86

Surprisingly, when the doping percentages in NNO thin films increases, a substantial Raman mode at 698.18 cm^{-1} appears. This Raman mode is absent in undoped NNO film, but it begins to appear at 5% Al doping and becomes highly prominent at 20% Al doping. Although this mode exists in $NdNi_{0.90}Al_{0.10}O_3$ films as well, it is weaker and more broadened. Charge disproportionation causes the formation of the Jahn-Teller Ni^{2+} ion, which can cause this mode to develop, especially in the insulating phase [2].

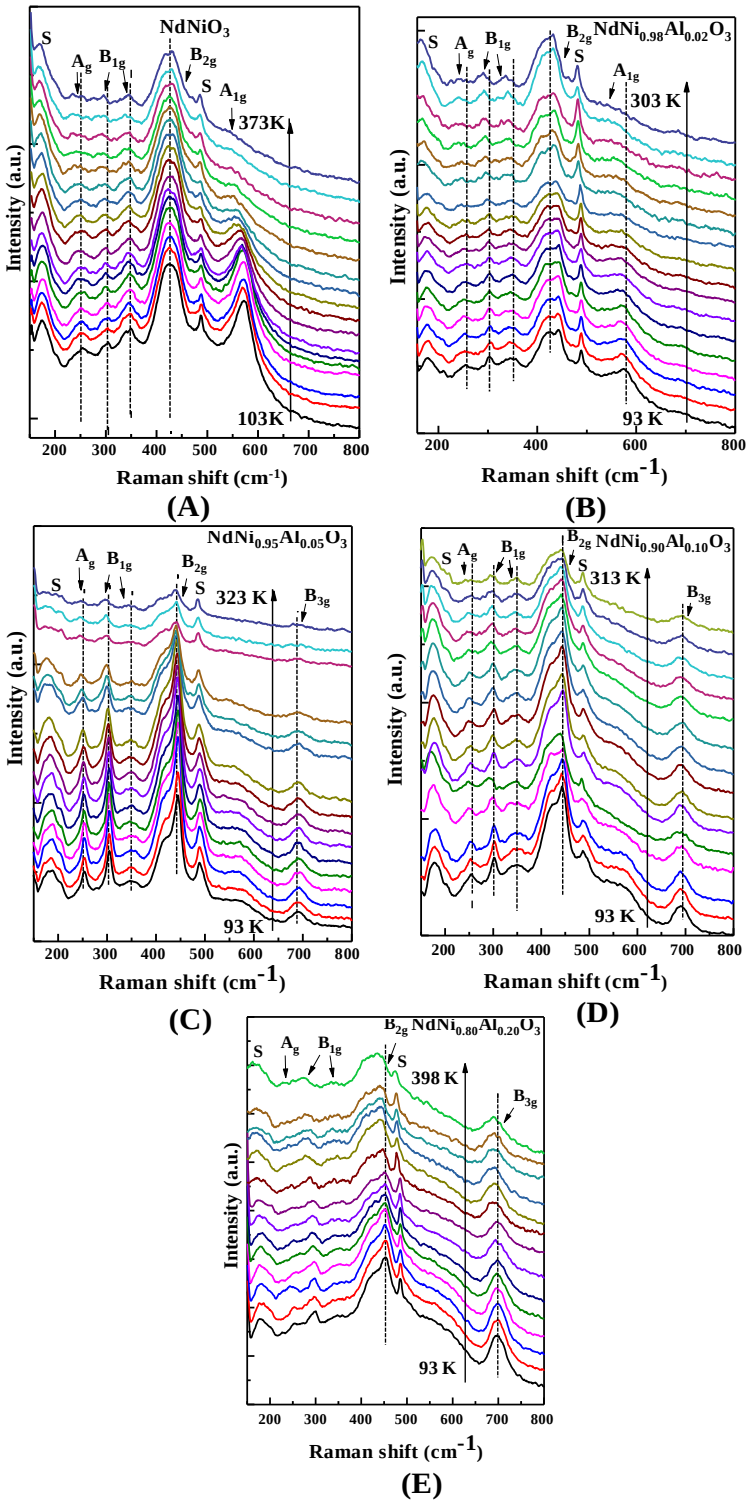

Figure 3.7: Temperature-dependent Raman spectra of $NdNi_{1-x}Al_xO_3$ (x = 0 - 0.2) thin films grown on LAO (001) substrate. The dashed line exhibits the shift in the modes.

In order to investigate more structural properties and phonon modes, we have performed thermal evolution of Raman spectroscopy as

shown in Figure-3.7. Different characteristics like as thermal expansion, anharmonicity, and others alter the vibrational and rotational modes of Raman spectra as temperature changes. These temperature-dependent Raman spectra reveal signs of symmetry breakdown, which is correlated to the transition from metal to insulator. The charge disproportionation occurs due to the variation of Ni^{3+}-O to $Ni^{3+\delta}/Ni^{3-\delta}$-O bond at the moment of phase transition. As a result of this variation, there exist two types of Ni-O bonds with differing bond lengths that cause the loss of the b mirror in the Pbnm space group and the structure in this Pbnm space group converts into $P2_1/n$ space group [2]. According to group theory, the ($7A_{1g}$ + $5B_{3g}$) and ($7B_{1g}$ + $5B_{2g}$) Raman modes associated with Pbnm space group are changed to $12A_g$ and $12B_g$ modes, respectively, during this structural phase transition [2]. This means that during this phase transition, no extra Raman mode affects Raman spectra. However, due to poor intensity peaks and peaks overlapping, some modes are not visible in our Raman spectra. The major peaks, according to our observations, are about 260, 305, 350, 425, 445, 480, 570, and 700 cm^{-1}. All the peaks observed in the particular temperature range shift towards lower wavenumbers that indicating the thermal expansion of interatomic bond length [3]. Thermal broadening of the peak at 445 cm^{-1} with the increment of temperature implies induced disorder in the structure due to sufficient thermal energy [3]. This red-shifting and thermal broadening in the B_{2g} peak at 445 cm^{-1} are consistent in the $NdNi_{0.95}Al_{0.05}O_3$ sample shown in Figure-3.8.

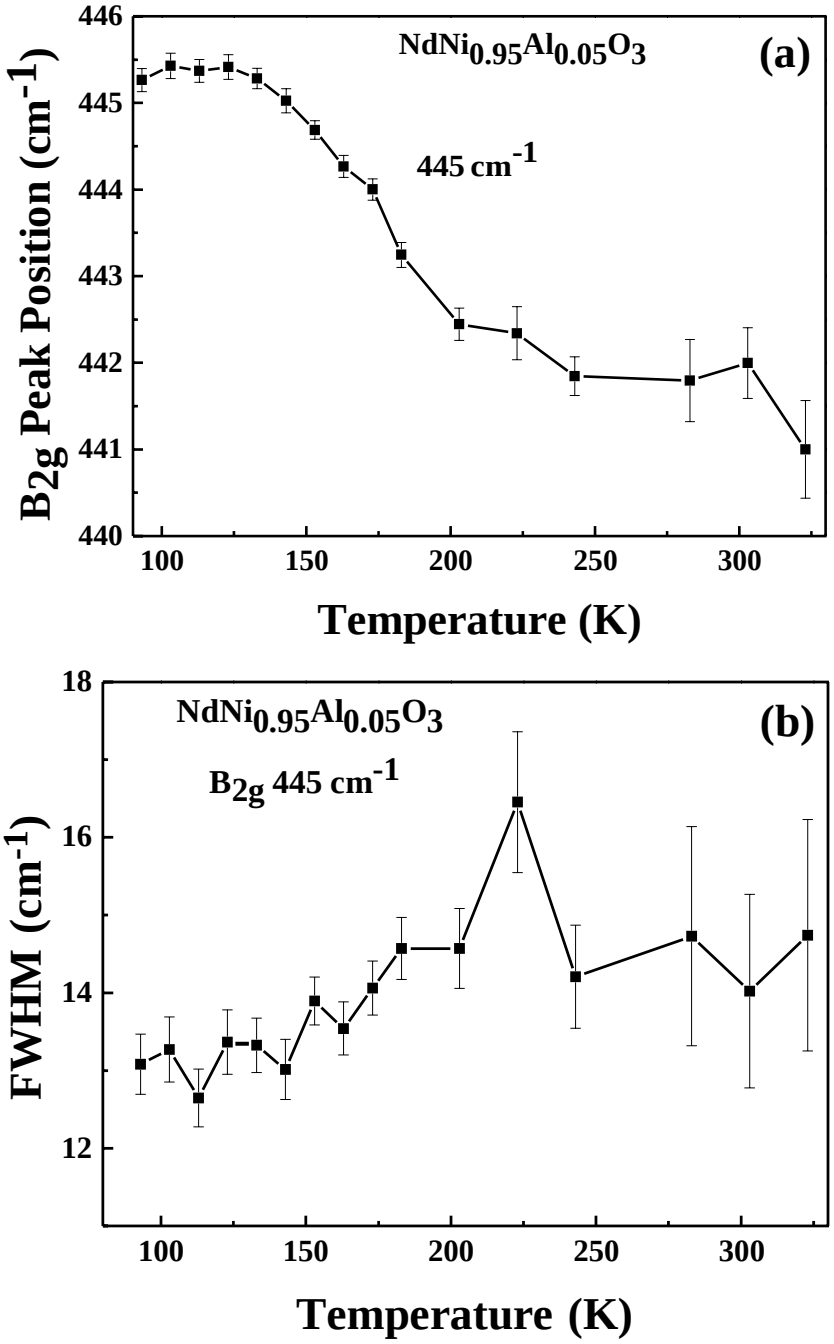

Figure 3.8: Shifting and broadening in B_{2g} Raman modes at 445 cm^{-1} with temperature for $NdNi_{0.95}Al_{0.05}O_3$ thin films grown on LAO (001) substrate

3.4 Conclusion:

The properties of Al-doped $NdNiO_3$ thin films have been studied with varying doping percentages. The out-of-plane parameters and lattice mismatch calculation confirm that the films experience an in-plane compressive strain. The increment of FWHM of XRD peaks and Room temperature Raman modes with doping percentages suggest that the disorder in the samples is superior as the doping percentages are increased. The blue shifting of the B_{2g} Raman mode at 427 cm^{-1} carries the information of enhancement of octahedral tilt angle with doping percentages. The red-shift of all modes in temperature-dependent Raman maintains the signature of thermal lengthening of inter-atomic bonds. Temperature-dependent resistivity data confirms the metal to insulator phase transition except for the $NdNi_{0.8}Al_{0.2}O_3$ sample. The $NdNi_{0.8}Al_{0.2}O_3$ thin film shows fully insulating behavior in the observed temperature range. The room temperature and temperature-dependent Raman study allow us to accept the charge ordering at Ni-site in our sample during the MIT which is also responsible for the structural transformation from orthorhombic to the monoclinic structure.

References:

[1] C. Girardot, J. Kreisel, S. Pignard, N. Caillault, and F. Weiss, “Raman scattering investigation across the magnetic and metal-insulator transition in rare earth nickelate R NiO3 (R=Sm, Nd) thin films,” *Physical Review B - Condensed Matter and Materials Physics*, vol. 78, no. 10, Sep. 2008, doi: 10.1103/PhysRevB.78.104101.

[2] M. Zaghrioui, A. Bulou, P. Lacorre, and P. Laffez, “Electron diffraction and Raman scattering evidence of a symmetry breaking at the metal-insulator transition of NdNiO3,” *Physical Review B - Condensed Matter and Materials Physics*, vol. 64, no. 8, pp. 811021–811024, Aug. 2001, doi: 10.1103/PhysRevB.64.081102.

[3] E. Yadav, K. Soni, S. Harisankar, S. Prabhu, and K. R. Mavani, “Influencing the structural, vibrational and electronic properties of pulsed laser deposited PrNi0.95Cu0.05O3 thin films by tuning epitaxial strain,” *Thin Solid Films*, vol. 735, Oct. 2021, doi: 10.1016/j.tsf.2021.138877.